Lattice calculation of the D_s meson radiative form factors over the full kinematical range

R. Frezzotti and N. Tantalo

Dipartimento di Fisica and INFN, Università di Roma "Tor Vergata", Via della Ricerca Scientifica 1,
I-00133 Rome, Italy

G. Gagliardi, F. Sanfilippo, and S. Simula

Istituto Nazionale di Fisica Nucleare, Sezione di Roma Tre, Via della Vasca Navale 84,
I-00146 Rome, Italy

V. Lubicz and F. Mazzetti

Dipartimento di Matematica e Fisica, Università Roma Tre and INFN,
Sezione di Roma Tre, Via della Vasca Navale 84, I-00146 Rome, Italy

G. Martinelli

Physics Department and INFN Sezione di Roma La Sapienza, Piazzale Aldo Moro 5, 00185 Rome, Italy

C. T. Sachrajda

Department of Physics and Astronomy, University of Southampton,
Southampton SO17 1BJ, United Kingdom

We compute the structure-dependent axial and vector form factors for the radiative leptonic decays $D_s \to \ell\nu_\ell\gamma$, where ℓ is a charged lepton, as functions of the energy of the photon in the rest frame of the D_s meson. We work in the electroquenched approximation, using gauge-field configurations with $2 + 1 + 1$ sea-quark flavors generated by the European Twisted Mass Collaboration and the results have been extrapolated to the continuum limit. For the vector form factor we observe a very significant partial cancellation between the contributions from the emission of the photon from the strange quark and that from the charm quark. The results for the form factors are used to test the reliability of various Anzätze based on single-pole dominance and its extensions, and we present a simple parametrization of the form factors which fits our data very well and which can be used in future phenomenological analyses. Using the form factors we compute the differential decay rate and the branching ratio for the process $D_s \to e\nu_e\gamma$ as a function of the lower cutoff on the photon energy. With a cutoff of 10 MeV for example, we find a branching ratio of $\mathrm{Br}(E_\gamma > 10 \text{ MeV}) = 4.4(3) \times 10^{-6}$ which, unlike some model calculations, is consistent with the upper bound from the BESIII experiment $\mathrm{Br}(E_\gamma > 10 \text{ MeV}) < 1.3 \times 10^{-4}$ at 90% confidence level. Even for photon energies as low as 10 MeV, the decay $D_s \to e\nu_e\gamma$ is dominated by the structure-dependent contribution to the amplitude (unlike the decays with $\ell = \mu$ or τ), confirming its value in searches for hypothetical new physics as well as in determining the Cabibbo-Kobayashi-Maskawa parameters at $O(\alpha_{\mathrm{em}})$, where α_{em} is the fine-structure constant.

I. INTRODUCTION

The comparison between experimental measurements and theoretical predictions for flavor-changing processes accompanied by photon emission represents an important tool in the search of new physics (NP) beyond the Standard Model (SM). In this paper we consider radiative weak leptonic decays of the form $P \to \ell\nu_\ell\gamma$, where P is a pseudoscalar

meson, $\ell\nu_\ell$ a lepton-neutrino pair, and γ a real photon. For each meson P, in addition to the leptonic decay constant f_P, the computation of the corresponding decay rate requires the calculation of two structure-dependent (SD) hadronic form factors, F_V and F_A, which depend on the energy of the photon in the meson rest frame. If instead the structure dependence of the meson is neglected, i.e. in the "pointlike" approximation, the only nonperturbative input required to determine the decay rate is f_P. An interesting feature of these decays is that, because of helicity suppression, the pointlike contribution to the decay rate is suppressed with respect to the SD contribution by the square of the ratio $r_\ell = m_\ell/m_P$, where m_ℓ and m_P are the masses of the charged lepton ℓ and meson P respectively. For heavy mesons P and light final-state charged leptons ℓ, the SD contribution, which is sensitive to the internal structure of the decaying meson, can already be dominant at relatively low photon energies, and in particular those well below the typical energy cutoff imposed in experimental measurements. This makes such decay channels an ideal place to probe the internal structure of the meson and the presence of possible NP contributions. While for pion and kaon decays several experimental measurements of the axial and vector form factors exist (see e.g. Refs. [1–6]), for heavy mesons only very little is known. For charmed meson decays the BESIII Collaboration recently searched for signals of the Cabibbo-suppressed decay $D^+ \to e^+\nu_e\gamma$ [7] and of the Cabibbo-favored one $D_s^+ \to e^+\nu_e\gamma$ [8], finding no events with emission of photons with energies $E_\gamma > 0.01$ GeV, and setting the following upper bounds on the branching ratios; $\mathrm{Br}[D \to e\nu_e\gamma] < 3 \times 10^{-5}$ and $\mathrm{Br}[D_s \to e\nu_e\gamma] < 1.3 \times 10^{-4}$ at 90% confidence level. For the B meson, the Belle Collaboration has recently set the bounds [9,10] $\mathrm{Br}[B \to e\nu_e\gamma] < 4.3 \times 10^{-6}$ and $\mathrm{Br}[B \to \mu\nu_\mu\gamma] < 3.4 \times 10^{-6}$, and observed photons with energies $E_\gamma > 1$ GeV. We believe that by providing accurate predictions from first principles for the axial and vector form factors for heavy mesons, we will motivate further experimental studies.

We have recently computed the rates for $P \to \ell\nu_\ell\gamma$ decays where P is a light meson, $P = \pi$ or K, [11] and compared our results to experimental measurements finding some puzzling and interesting discrepancies yet to be resolved [12]. In Ref. [11] we have also computed the amplitude for the decays of the D_s meson, but only over part of the physical phase space; specifically for photon energies up to 0.4 GeV, as measured in the rest frame of the D_s meson. In this paper, we return to the radiative decays of D_s mesons and compute the relevant axial and vector form factors F_V and F_A over the full physical kinematic range and with high-statistical accuracy, thus improving significantly upon the previous study of Ref. [11]. The computation is performed using the $N_f = 2 + 1 + 1$ Wilson-Clover twisted-mass gauge ensembles generated by the Extended Twisted Mass Collaboration (ETMC)

with quark masses tuned very close to their physical values, for almost all the ensembles [13–16]. The ensembles correspond to four values of the lattice spacing a in the range $[0.56, 0.9]$ fm, with the spatial extent of the lattice, L, ranging from 4.4 fm to 7.6 fm.

Our main results for the D_s radiative form factors F_V and F_A are collected in Table V and plotted in Fig. 8, and we provide their correlation matrices in Appendix B. Recently, numerical results for the lattice computation of F_V and F_A of the D_s meson also have been published in Ref. [17]. The primary focus of that paper however, is on developing and testing different strategies for the lattice computation of the form factors. Their numerical results are based on a single-gauge ensemble at an unphysical pion mass, and for this reason a direct comparison with our results is not possible at present. In the future, it would be interesting to compare our results with those obtained from other lattice regularizations in the continuum limit.

We use our results for the form factors to compute the branching fraction of the $D_s \to e^+\nu_e\gamma$ decay, as a function of the lower cutoff, ΔE_γ, on the photon energy, as measured in the meson rest frame. Our results are showed in Fig. 10. For $\Delta E_\gamma = 0.01$ GeV, our prediction for the branching fraction lies well below the experimental upper limit set by the BESIII Collaboration [8]. Due to the strong helicity suppression, the branching fraction is dominated by the SD contribution, even for a lower cut on the photon energy as small as 0.01 GeV. In Fig. 11, we show the SD contribution to the differential $D_s \to e^+\nu_e\gamma$ decay rate, as a function of the photon energy in the meson rest frame; this goes to zero at the edge of phase space and reaches a maximum in the region kinematic $x_\gamma \equiv 2E_\gamma/M_{D_s} \simeq 0.6$–$0.7$.

Having calculated the form factors from first principles in a lattice computation, we test how well model calculations based on single-pole dominance and light cone sum rules (LCSR) reproduce our results. Such a test is important because model calculations are commonly used to describe the form factors of heavy mesons, in particular the B meson [18–20], for which a direct lattice calculation is currently missing. We fit our results for the vector and axial form factors of the D_s meson to several polelike Ansätze, finding that, in general, a pure vector-meson-dominance (VMD) Ansatz does not describe very well the momentum dependence of the data, particularly for the axial form factor F_A. However, by including the leading nonsingular corrections in the Laurent expansion around the pole, we obtain a very good description of our lattice data. The resulting fit parameters are collected in Table VI and can be used for future phenomenological analyses.

From the polelike fits to F_V we extract the coupling $g_{D_s^* D_s \gamma}$, which is the form factor describing the $D_s^* \to D_s\gamma$ decay. Our estimate of $g_{D_s^* D_s \gamma}$ is in good agreement with the direct lattice determination of Ref. [21] but strongly disagrees with the value predicted by light cone sum rules (LCSR) at next-to-leading order (NLO) [22], from which it

differs by a factor 5. LCSR at NLO order were also used to estimate the radiative form factors F_V and F_A of the D_s meson, at one specific kinematical point [23]. Their estimates disagree very significantly with those from our direct lattice computation, differing by a factor 4 for the vector form factor F_V, and by an order of magnitude and a relative minus sign, for the axial form factor F_A. We conclude that caution should be exercised when using such calculations based on LCSR to predict the heavy-meson radiative form factors. A similar message is conveyed in a recent paper on the $B_s \to \mu^+\mu^-\gamma$ decay [24].

The plan for the remainder of this paper is as follows. In Sec. II we explain how the two structure dependent form factors contributing to the amplitude for $D_s^+ \to \ell^+\nu_\ell\gamma$ decays, F_V and F_A, can be determined from suitable Euclidean lattice correlation functions. In Sec. III we briefly describe the mixed-action lattice framework which we use and present detailed information on the technical aspects of the simulations. Section IV contains the determination of the form factors, together with our estimates of the systematic errors, including a description of the extrapolations to the continuum and infinite volume limits. In this section we also present the determination of the differential decay rate and branching fraction, as a function of ΔE_γ, for the $D_s \to e\nu_e\gamma$ decay. In Sec. V we provide a simple polelike parametrization of our data for F_V and F_A, which may be useful for those interested in using our data for phenomenological analyses. We also compare the results presented in Sec. IV with predictions from models based on pole dominance or light-cone sum-rules. Finally in Sec. VI we present our conclusions. There are three appendixes to supplement the information in the main text. In Appendix A we explain the reason for the observed deterioration of the signal-to-noise ratio at large photon energies. The results for the form factors F_V and F_A, together with the corresponding correlation matrices are tabulated in Appendix B so that they can be used in phenomenological studies. In Appendix C we present a detailed analysis of single-pole parametrizations of our results for the form factors.

II. DEFINITION OF THE FORM FACTORS

In order to make this paper self contained, in this section we briefly summarize our conventions and notation, and in particular recall the definition of the structure-dependent form factors which had previously been introduced in Refs. [11,25–27]. The nonperturbative contribution to the radiative leptonic decay rate for the processes $D_s^+ \to \ell^+\nu_\ell\gamma$ is encoded in the hadronic matrix element

$$H_W^{r\nu}(k, \boldsymbol{p}) = \epsilon_\mu^r(k) H_W^{\mu\nu}(k, \boldsymbol{p})$$
$$= \epsilon_\mu^r(k) \int d^4 y\, e^{ik\cdot y} \langle 0|\hat{\mathrm{T}}[j_W^\nu(0) j_{\mathrm{em}}^\mu(y)]|D_s^+(\boldsymbol{p})\rangle, \tag{1}$$

where $\hat{\mathrm{T}}$ implies time ordering of the two currents, ϵ_μ^r is the polarization vector of the outgoing photon with four-momentum k, $\boldsymbol{p}$ is the three-momentum of the D_s meson, and $j_W^\nu(x)$ and $j_{\mathrm{em}}^\mu(x)$ are the weak- and electromagnetic-hadronic currents respectively:

$$j_W^\nu(x) = j_V^\nu(x) - j_A^\nu(x) = \bar{\psi}_s(x)(\gamma^\nu - \gamma^\nu\gamma_5)\psi_c(x),$$
$$j_{\mathrm{em}}^\mu(x) = \sum_f q_f \bar{\psi}_f(x)\gamma^\mu\psi_f(x), \tag{2}$$

where q_f is the electric charge of the flavor f. The hadronic tensor $H_W^{\mu\nu}$ can be decomposed in terms of a "pointlike" contribution $H_{\mathrm{pt}}^{\mu\nu}$ (i.e. the expression obtained by treating the D_s meson as a pointlike particle) and four structure-dependent (SD) scalar form factors, F_V, F_A, H_1 and H_2 [11,25–27][1]:

$$H_W^{\mu\nu}(k, \boldsymbol{p}) = H_{\mathrm{SD}}^{\mu\nu}(k, \boldsymbol{p}) + H_{\mathrm{pt}}^{\mu\nu}(k, \boldsymbol{p}) \tag{3}$$

$$H_{\mathrm{SD}}^{\mu\nu}(k, \boldsymbol{p}) = \frac{H_1(p\cdot k, k^2)}{M_{D_s}}[k^2 g^{\mu\nu} - k^\mu k^\nu] + \frac{H_2(p\cdot k, k^2)}{M_{D_s}}$$
$$\times \frac{[(p\cdot k - k^2)k^\mu - k^2(p-k)^\mu]}{(p-k)^2 - M_{D_s}^2}(p-k)^\nu$$
$$- i\frac{F_V(p\cdot k, k^2)}{M_{D_s}}\epsilon^{\mu\nu\gamma\beta}k_\gamma p_\beta + \frac{F_A(p\cdot k, k^2)}{M_{D_s}}$$
$$\times [(p\cdot k - k^2)g^{\mu\nu} - (p-k)^\mu k^\nu] \tag{4}$$

$$H_{\mathrm{pt}}^{\mu\nu}(k, \boldsymbol{p}) = f_{D_s}\left[g^{\mu\nu} + \frac{(2p-k)^\mu(p-k)^\nu}{2p\cdot k - k^2}\right], \tag{5}$$

where M_{D_s} is the mass of the D_s meson and $p = (E, \boldsymbol{p})$ its four momentum, with $E = \sqrt{M_{D_s}^2 + \boldsymbol{p}^2}$. The pointlike contribution $H_{\mathrm{pt}}^{\mu\nu}$ saturates the Ward identity (WI) satisfied by $H_W^{\mu\nu}$:

$$k_\mu H_W^{\mu\nu}(k, \boldsymbol{p}) = k_\mu H_{\mathrm{pt}}^{\mu\nu}(k, \boldsymbol{p}) = i\langle 0|j_W^\nu(0)|D_s^+(\boldsymbol{p})\rangle = f_{D_s}p^\nu. \tag{6}$$

which implies that $k_\mu H_{\mathrm{SD}}^{\mu\nu}(k, \boldsymbol{p}) = 0$. Moreover, when integrating over the full three-body phase space, it is only the square of the pointlike term which is infrared divergent. At order $O(\alpha_{\mathrm{em}})$, this infrared divergence is canceled by the virtual photon correction to the purely leptonic decay.

Equation (5) is valid for generic (off shell) values of the photon four-momentum k and can also be used to

---

[1]Here, we use the dimensionless definitions of $H_{1,2}$ introduced in Ref. [27] which differ by simple factors from those used in our earlier papers [11,25]. As explained below, the form factors $H_{1,2}$ do not contribute to the decays studied here, i.e. those with a real photon in the final state.

study the four-body decay $D_s^+ \to \ell^+ \nu_\ell \ell'^+ \ell'^-$, where the ℓ' are charged leptons, or more generally the decays $P \to \ell \nu_\ell \ell'^+ \ell'^-$ of any pseudoscalar meson P, as we showed in an exploratory work with $P = K$ [27]. In this paper we study the emission of a real photon, so that $k^2 = 0$ and $\epsilon^r \cdot k = 0$, and therefore only the axial form factor $F_A(p \cdot k)$ and the vector form factor $F_V(p \cdot k)$, together with the pointlike term, contribute to the decay rate for the process $D_s^+ \to \ell^+ \nu_\ell \gamma$.

In the following, as in our previous study [11], we find it convenient to evaluate the form factors F_V and F_A as functions of the dimensionless variable

$$x_\gamma \equiv \frac{2p \cdot k}{M_{D_s}^2}; \qquad 0 \le x_\gamma \le 1 - \frac{m_\ell^2}{M_{D_s}^2} < 1, \qquad (7)$$

where m_ℓ is the mass of the charged lepton ℓ. In the rest frame of the D_s meson ($\boldsymbol{p} = \boldsymbol{0}$) $x_\gamma = 2E_\gamma/M_{D_s}$, where E_γ is the energy of the photon. The above discussion applies to other pseudoscalar mesons (π, K, D, $B_{(s)}$) with the natural replacement of D_s in Eqs. (1)–(7) by the meson being studied and the corresponding change of the quark flavors in the weak current in Eq. (2).

A. Evaluating F_V and F_A from Euclidean lattice-correlation functions

In Sec. III and Appendix B of Ref. [11] we showed in detail that for the emission of a real photon, the hadronic tensor $H_W^{\mu\nu}$ can be extracted for all values of x_γ from the Euclidean three-point correlation function:

$$C_W^{\mu\nu}(t; k, p) = -i \sum_{t_y=0}^{T} \sum_{\boldsymbol{y}} \sum_{\boldsymbol{x}} (\theta(T/2 - t_y)$$
$$+ \theta(t_y - T/2) e^{-E_\gamma T}) e^{t_y E_\gamma - i\boldsymbol{k}\cdot\boldsymbol{y} + i\boldsymbol{p}\cdot\boldsymbol{x}}$$
$$\times \langle 0|\hat{\mathrm{T}}[j_W^\nu(t,\boldsymbol{0}) j_{\mathrm{em}}^\mu(t_y,\boldsymbol{y}) \phi_{D_s}^\dagger(0,\boldsymbol{x})]|0\rangle, \quad (8)$$

where T is the temporal extent of the lattice,[2] $\phi_{D_s}^\dagger$ is an interpolating operator with the quantum numbers to create the D_s meson, $k = (E_\gamma, \boldsymbol{k})$, and E_γ is the energy of the photon. In the forward half of the lattice $0 \ll t \ll T/2$ for example, one has

$$R_W^{\mu\nu}(t; E_\gamma, \boldsymbol{k}, \boldsymbol{p}) \equiv \frac{2E}{e^{-t(E-E_\gamma)} \langle D_s(\boldsymbol{p})|\phi_{D_s}^\dagger(0)|0\rangle} C_W^{\mu\nu}(t, E_\gamma, \boldsymbol{k}, \boldsymbol{p})$$
$$= H_W^{\mu\nu}(k, \boldsymbol{p}) + \cdots, \qquad (9)$$

where the ellipsis indicates terms that vanish exponentially in the large t limit and $E = \sqrt{\boldsymbol{p}^2 + M_{D_s}^2}$. Equation (8) is

---

[2]T is not to be confused with $\hat{\mathrm{T}}$ which represents "time ordered".

valid for $t < T/2$, however, as explained in Appendix B of Ref. [11], $H_W^{\mu\nu}(k, \boldsymbol{p})$ can be obtained also from the backward half of the lattice $T/2 \ll t \ll T$ exploiting time-reversal symmetry. In order to determine the form factors F_V and F_A it is convenient to distinguish the contributions from the vector and axial-vector components of the weak current, $j_W^\nu = V^\nu - A^\nu$, and to write

$$R_W^{\mu\nu}(t; E_\gamma, \boldsymbol{k}, \boldsymbol{p}) = R_V^{\mu\nu}(t; E_\gamma, \boldsymbol{k}, \boldsymbol{p}) - R_A^{\mu\nu}(t; E_\gamma, \boldsymbol{k}, \boldsymbol{p}). \quad (10)$$

The Wick contractions of the correlation function in Eq. (8) give rise to two distinct topologies of Feynman diagrams, namely to quark-line connected and quark-line disconnected diagrams; these are illustrated in Fig. 1. In the disconnected diagrams the photon is emitted from a sea quark. This contribution vanishes in the SU(3)-symmetric limit and is neglected in the present study; this is the so-called electroquenched approximation. We focus instead on the calculation of the dominant, quark-connected contributions for which as explained in Ref. [11], it is possible to use twisted boundary conditions to assign arbitrary values to momenta of the photon and D_s-meson, $\boldsymbol{k}$ and $\boldsymbol{p}$ respectively, at the price of violations of unitarity which vanish exponentially with the lattice extent L [28,29]. This is achieved by treating the two quark propagators related to the electromagnetic current in the right-hand diagram of Fig. 1 as corresponding to two distinct quark fields ψ^0, ψ^t having the same mass and quantum number, but satisfying different spatial boundary conditions. Defining ψ^s to be the *spectator* quark-field in the right-hand diagram of Fig. 1, we set the spatial boundary conditions of the three quark fields ψ^0, ψ^t, ψ^s as follows:

$$\psi^r(x + \boldsymbol{n}L) = \exp(2\pi i \boldsymbol{n} \cdot \boldsymbol{\theta}_r) \psi^r(x), \qquad r = \{0, t, s\}, \quad (11)$$

where $\boldsymbol{\theta}_{\{0,t,s\}}$ are arbitrary spatial-vectors of angles, in terms of which the photon and meson lattice momenta are given by

$$\boldsymbol{p} = \frac{2}{a} \sin\left(\frac{a\pi}{L}(\boldsymbol{\theta}_0 - \boldsymbol{\theta}_s)\right), \qquad \boldsymbol{k} = \frac{2}{a} \sin\left(\frac{a\pi}{L}(\boldsymbol{\theta}_0 - \boldsymbol{\theta}_t)\right), \quad (12)$$

where a is the lattice spacing. The results presented in the following sections have been obtained in the rest frame of the D_s meson ($\boldsymbol{p} = \boldsymbol{0}$) and with the photon momentum chosen to be in the z-direction, $\boldsymbol{k} = (0, 0, k_z)$, i.e. by setting

$$\boldsymbol{\theta}_0 = \boldsymbol{\theta}_s = \boldsymbol{0}, \qquad \boldsymbol{\theta}_t = (0, 0, \theta_t). \quad (13)$$

With such a choice of kinematics, the two form factors F_V and F_A can be obtained from the large-time behavior, $0 \ll t \ll T/2$, of the following two estimators:
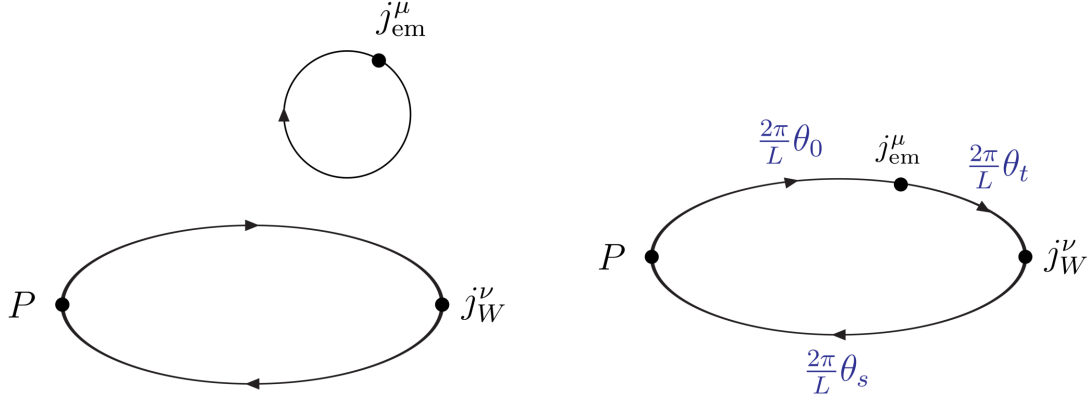
FIG. 1.   The diagram on the left represents the quark-line disconnected contributions to the correlation function $C_W^{\mu\nu}$ in which the photon is emitted by a sea quark. In our numerical simulations we work in the electroquenched approximation and neglect such diagrams. The one on the right represents the quark-line connected contributions and illustrates our choice of the spatial boundary conditions, which allow us to set arbitrary values for the meson and photon spatial momenta. The spatial momenta of the valence quarks, modulo $2\pi/L$, in terms of the twisting angles are as indicated. Each diagram implicitly includes all orders in QCD.

$$R_V(t,\boldsymbol{k}) \equiv \frac{1}{2k_z}\left(R_V^{12}(t,\boldsymbol{k},\boldsymbol{0}) - R_V^{21}(t,\boldsymbol{k},\boldsymbol{0})\right)\xrightarrow[0\ll t\ll T/2]{} F_V(x_\gamma),$$

$$(14)$$

$$R_A(t,\boldsymbol{k}) \equiv \frac{1}{2E_\gamma}\left[(R_A^{11}(t,\boldsymbol{k},\boldsymbol{0}) - R_A^{11}(t,\boldsymbol{0},\boldsymbol{0})) + (R_A^{22}(t,\boldsymbol{k},\boldsymbol{0})\right.$$
$$\left. - R_A^{22}(t,\boldsymbol{0},\boldsymbol{0}))\right]\xrightarrow[0\ll t\ll T/2]{} F_A(x_\gamma),\quad (15)$$

where $x_\gamma = 2E_\gamma/M_P$ and, since for a real photon E_γ is determined by $\boldsymbol{k}$, we have redefined

$$R_{V,A}^{\mu\nu}(t,\boldsymbol{k},\boldsymbol{0}) \equiv R_{V,A}^{\mu\nu}(t,E_\gamma(\boldsymbol{k}),\boldsymbol{k},\boldsymbol{0}),$$
$$E_\gamma(\boldsymbol{k}) = \frac{2}{a}\sinh^{-1}\left(\frac{a|\boldsymbol{k}|}{2}\right),\quad (16)$$

where we used the lattice dispersion relation for the photon energy. Notice that in the estimator $R_A(t,\boldsymbol{k})$ of the axial form factor, the zero-momentum subtraction serves to remove the pointlike contribution proportional to f_P. As discussed in Sec. IV of Ref. [11], the subtractions in Eq. (15) of R_A^{11} and R_A^{22} at $\boldsymbol{k} = \boldsymbol{0}$ allow us to isolate the SD form factor $F_A(x_\gamma)$ without generating infrared-divergent cutoff effects of order $\mathcal{O}(a^2/x_\gamma)$. Such dangerous discretization effects, which could hinder the determination of $F_A(x_\gamma)$ at small values of x_γ, are present instead if one subtracts the pointlike contribution $H_{\mathrm{pt}}^{\mu\nu}$ in Eq. (1), using the value of the decay constant f_{D_s} determined from two-point correlation functions.

III. DETAILS OF THE COMPUTATION

Our results have been obtained using the gauge field configurations generated by the ETMC employing the Iwasaki gluon action [30] and $N_f = 2 + 1 + 1$ flavors of

Wilson-Clover twisted-mass fermions at maximal twist [31]. This framework guarantees the automatic $\mathcal{O}(a)$ improvement of parity-even observables [32,33]. A detailed description of the ETMC ensembles can be found in Refs. [13–16], while essential informations on the ensembles we have used in the present work are collected in Table I. The ensembles listed in Table I correspond to four values of the lattice spacing a in the range $[0.058, 0.09]$ fm, and lattice extent L in the range $[4.36, 5.46]$ fm. The mass of the light sea quarks on the three finest ensembles, has been tuned so as to give almost physical-mass pions, while on the coarsest ensemble the pion mass[3] is $M_\pi \simeq 175$ MeV. For all the ensembles, the strange and charm sea-quark masses are set to within about 5% of their physical values, defined through the requirement that (see Refs. [13,14,16] for more details)

$$\frac{M_{D_s}}{f_{D_s}} = 7.9 \pm 0.1, \qquad \frac{m_c}{m_s} = 11.8 \pm 0.2. \quad (17)$$

We work in a mixed-action framework in which the valence strange and charm quarks are discretized as Osterwalder-Seiler fermions [33,35]. The corresponding valence bare-quark mass parameters μ_s and μ_c, have been tuned to reproduce the value of the pseudoscalar $\eta_{ss'}$ mass[4] determined in Ref. [36] and the PDG value [37] of the pseudoscalar η_c mass (see Appendix C of Ref. [16] for more details)

---

[3]For the present study of the D_s meson, the presence of a heavier-than-physical pion, with mass $M_\pi \simeq 175$ MeV, on the coarsest ensemble does not require a chiral extrapolation since we expect that the form factors are largely insensitive to the value of the masses of the light sea quarks.

[4]The $\eta_{ss'}$ is a fictitious pseudoscalar meson made of two different mass-degenerate quarks s and s' having mass equal to that of the strange quark. Its mass is equivalent to that of the $\bar{s}\gamma^5 s$ meson if one neglects quark-line disconnected contributions.

TABLE I. Parameters of the ETMC ensembles used in this work. We present the light-quark bare mass, $a\mu_\ell = a\mu_u = a\mu_d$, the lattice spacing a, the pion mass M_π, the lattice size L, and the number of gauge configurations N_g that have been used for each ensemble. The values of the lattice spacing are determined as explained in Appendix B of Ref. [16] using the 2016 PDG value $f_\pi^{\text{phys}} = f_\pi^{\text{isoQCD}} = 130.4(2)$ MeV [34] of the pion decay constant.

Ensemble	β	V/a^4	a (fm)	$a\mu_\ell$	M_π (MeV)	L (fm)	N_g
cA211.12.48	1.726	$48^3 \cdot 128$	0.09075 (54)	0.00120	174.5 (1.1)	4.36	109
cB211.072.64	1.778	$64^3 \cdot 128$	0.07957 (13)	0.00072	140.2 (0.2)	5.09	199
cC211.060.80	1.836	$80^3 \cdot 160$	0.06821 (13)	0.00060	136.7 (0.2)	5.46	72
cD211.054.96	1.900	$96^3 \cdot 192$	0.05692 (12)	0.00054	140.8 (0.2)	5.46	100

$$M_{\eta_{ss'}}^{\text{phys}} = 689.89(49) \text{ MeV}, \qquad M_{\eta_c}^{\text{phys}} = 2.984(4) \text{ GeV}, \tag{18}$$

$$
\begin{aligned}
j_W^\nu(t,\boldsymbol{x}) &= j_V^\nu(t,\boldsymbol{x}) - j_A^\nu(t,\boldsymbol{x}) = Z_A j_V^{\nu,\text{bare}} - Z_V j_A^{\nu,\text{bare}} \\
&= Z_A \bar{\psi}_s(t,\boldsymbol{x}) \gamma^\nu \psi_c(t,\boldsymbol{x}) - Z_V \bar{\psi}_s(t,\boldsymbol{x}) \gamma^\nu \gamma_5 \psi_c(t,\boldsymbol{x}).
\end{aligned}
\tag{19}
$$

where the error in $M_{\eta_c}^{\text{phys}}$ includes, in addition to the experimental uncertainty, an estimate of the contribution from the neglected disconnected diagrams [38,39]. The values of μ_s and μ_c used for each of the ensembles of Table I are collected in Table II. Since the strange and charm quark masses have been fixed using the mass of the $\eta_{ss'}$ and η_c mesons, the mass of the D_s meson deviates from the physical value by $\mathcal{O}(a^2)$ cutoff effects, as we show in Fig. 2.

On each ensemble, we have analyzed $\mathcal{O}(100)$ gauge configurations and performed the inversions of the Dirac operator on four stochastic sources. The sources are randomly distributed over time, diagonal in spin and dense in the color. The interpolating operator $\phi_{D_s}^\dagger(0)$ has been smeared as in our previous works using Gaussian smearing (see e.g. Ref. [40] for more details). We employ a local discretization of the weak current,

Note that at maximal twist the renormalization constants (RCs) to be used for $j_V^{\nu,\text{bare}}$ and $j_A^{\nu,\text{bare}}$ are chirally rotated with respect to the ones of standard Wilson fermions, and the bare vector ($j_V^{\nu,\text{bare}}$) and axial-vector ($j_A^{\nu,\text{bare}}$) currents renormalize respectively with multiplicative renormalization constants Z_A and Z_V. For the electromagnetic current j_{em}^μ, we use the exactly-conserved point-split current

$$
\begin{aligned}
j_{\text{em}}^\mu(x) = -\sum_f q_f \Big\{ &\bar{\psi}_f(x) \frac{i r_f \gamma_5 - \gamma^\mu}{2} U^\mu(x) \psi_f(x+\hat{\mu}) \\
&- \bar{\psi}_f(x+\hat{\mu}) \frac{i r_f \gamma_5 + \gamma^\mu}{2} U^\mu(x)^\dagger \psi_f(x) \Big\},
\end{aligned}
\tag{20}
$$

where $U^\mu(x)$ are the QCD gauge links, and $r_f = \pm 1$ is the sign of the chirally-rotated Wilson term used for flavor f. In the electroquenched approximation only the $f = s$ and
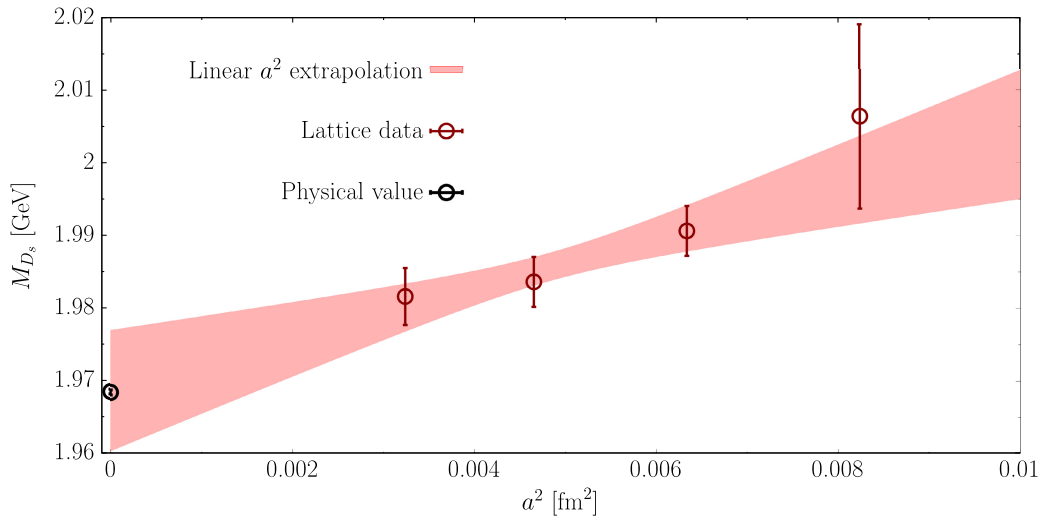

FIG. 2. The value of the D_s meson mass on the ensembles of Table I is plotted as a function of squared lattice spacing. The red band corresponds to the result of the continuum extrapolation using a linear fit Ansatz in a^2. The black data point at $a^2 = 0$ is the experimental value $M_{D_s}^{\text{exp}} = 1.96847(33)$ GeV.

TABLE II. Values of the bare valence-quark masses μ_s and μ_c in lattice units used for each ETMC ensemble considered in this work. They have been determined imposing the conditions in Eq. (18).

Ensemble	$a\mu_s$	$a\mu_c$
cA211.12.48	0.0200	0.2725
cB211.072.64	0.0184	0.2370
cC211.060.80	0.0162	0.2019
cD211.054.96	0.0136	0.1671

TABLE III. The values of Z_A/Z_V used in the evaluation of $\bar{R}_V(t, \mathbf{k})$ are given for each of the gauge ensembles of Table I.

Ensemble	Z_A/Z_V
cA211.12.48	1.0603 (26)
cB211.072.64	1.05176 (35)
cC211.060.80	1.04535 (22)
cD211.054.96	1.04011 (16)

$f = c$ terms in $j_{\rm em}^\mu$ contribute to the correlation function in Eq. (8). In our numerical simulations, we have chosen opposite signs for the chirally-rotated twisted term of the strange and charm valence quarks, $r_c = -r_s = 1$. We evaluate the correlation functions $C_W^{\mu\nu}$ in Eq. (8) and the estimators $R_W^{\mu\nu}$ in Eq. (9) using the bare currents $j_{V,A}^{\nu,\rm bare}$ in Eq. (19) and the point-split electromagnetic current in Eq. (20).

The RC Z_V which renormalizes the current $j_A^{\nu,\rm bare}$, is determined from the large-time behavior of the following estimator:

$$\bar{Z}_V(t) = -\frac{2f_{D_s}}{\sum_{i=1,2} R_A^{ii}(t,0,0)} \xrightarrow[0 \ll t \ll T]{} Z_V. \qquad (21)$$

In the twisted-mass framework which we are using, the decay constant f_{D_s} can be determined from the large-time behavior of the two-point correlation function $C_{PP}(t)$, without the need of additional renormalization, using

$$C_{PP}(t) \equiv \sum_{\mathbf{x}} \langle 0|(\bar{\psi}_s(t,\mathbf{x})\gamma^5\psi_c(t,\mathbf{x}))(\bar{\psi}_c(0)\gamma^5\psi_s(0))|0\rangle$$

$$\xrightarrow[0 \ll t \ll T]{} |\mathcal{Z}|^2 \frac{e^{-M_{D_s}T/2}}{2M_{D_s}} \cosh\left(M_{D_s}(t - T/2)\right), \qquad (22)$$

and

$$f_{D_s} = \sqrt{|\mathcal{Z}|^2} \frac{a\mu_s + a\mu_c}{M_{D_s}\sinh aM_{D_s}}, \qquad (23)$$

where the strange and charm quark fields entering $C_{PP}(t)$ in Eq. (22) carry opposite signs of the chirally-rotated twisted term. In practice, we find it convenient to define the following estimators to extract the physical form factors F_V and F_A

$$\bar{R}_A(t,\mathbf{k}) = \bar{Z}_V(t)R_A(t,\mathbf{k}), \quad \bar{R}_V(t,\mathbf{k}) = \frac{Z_A}{Z_V}\bar{Z}_V(t)R_V(t,\mathbf{k}), \qquad (24)$$

where the values of the ratio Z_A/Z_V used for each of the ensembles in Table I, are taken from the analysis of Ref. [16], and reported in Table III.

IV. NUMERICAL RESULTS

In this section we present the numerical results for the form factors F_A and F_V at ten evenly spaced values of x_γ (Sec. IV A). We then use these results to calculate the differential decay rate and branching fraction for the process $D_s^+ \to e^+\nu_e\gamma$ (Sec. IV B).

A. Results for the form factors

In order to determine the form factors, we evaluate the estimators $\bar{R}_{A,V}(t,\mathbf{k})$ at ten evenly-spaced values of the dimensionless variable x_γ:

$$x_\gamma = \frac{2E_\gamma}{M_{D_s}} = n\Delta x_\gamma, \qquad \Delta x_\gamma = 0.1, \qquad n \in \{1, \ldots, 10\}. \qquad (25)$$

At finite lattice spacing a, the relations between the twist angle θ_t, the photon momentum $\vec{k} = (0, 0, k_z)$ and x_γ are obtained from Eqs. (12) and (16),

$$k_z = -\frac{2}{a}\sin\left(\frac{a\pi}{L}\theta_t\right), \qquad x_\gamma = \frac{4}{aM_{D_s}}\sinh^{-1}\left(\frac{a|k_z|}{2}\right). \qquad (26)$$

For each gauge ensemble, we obtain each of the values of x_γ by tuning the twisting angle θ_t using the relations in Eq. (26) and the value of aM_{D_s}. The resulting statistical uncertainty on the values of x_γ is negligibly small [typically below $\mathcal{O}(0.1\%)$]. For an illustration of the quality of the plateaus, we present in Figs. 3 and 4 the estimators $\bar{R}_{V,A}(t, x_\gamma) \equiv \bar{R}_{V,A}(t, (0, 0, k_z(x_\gamma))$ for selected values of x_γ, obtained on the ensembles cB211.072.64 (B64 for short) and cC211.06.80 (C80 for short) respectively. In each figure the blue band shows the values of $F_{V,A}$ obtained from a constant fit in the region where the estimators $\bar{R}_{A,V}(t, x_\gamma)$ display a plateau.[5] As is clear from the figures, we observe a rapid deterioration of the signal for both F_V and F_A at large values of $x_\gamma \gtrsim 0.7$. In particular the

---

[5] We have checked that the results are stable under small shifts, in both forward and backward direction, of the time intervals adopted in the constant fit.
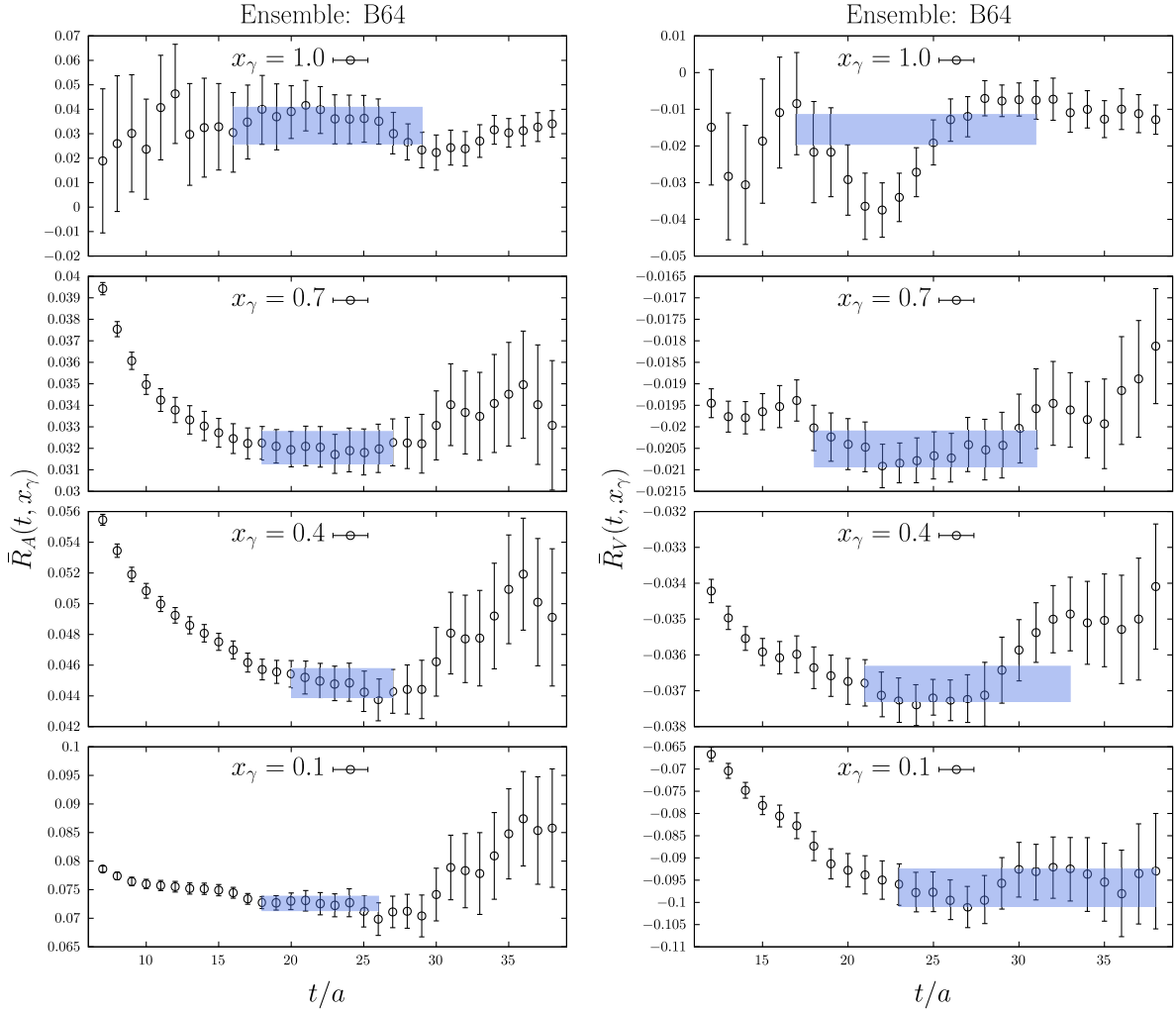
FIG. 3.   The estimators $\bar{R}_A(t, x_\gamma)$ and $\bar{R}_V(t, x_\gamma)$ as a function of t/a for selected values of x_γ on the ensemble B64. In each figure the blue band corresponds to the result of a constant fit over the indicated region.

statistical errors on $\bar{R}_{A,V}(t, x_\gamma > 0.8)$ turn out to be very large at small values of t/a, and then progressively decrease as t/a increases. The origin of this peculiar behavior, which is discussed in detail in Appendix A, is due to the existence of a threshold value of E_γ above which the intrinsic statistical fluctuations of $R_W^{\mu\nu}$ start to grow asymptotically with E_γ. As argued in Appendix A, this threshold value of E_γ is given by the mass $M_{\bar{q}q}^{\text{PS}}$ of the lightest pseudoscalar meson state $\bar{\psi}_q \gamma^5 \psi_q$ with $q = U, D$. The outcome of the analysis is that for $E_\gamma > M_{\bar{q}q}^{\text{PS}}$, the fluctuation $\sigma_{R_W^{\mu\nu}}$ of $R_W^{\mu\nu}$ scales asymptotically as

$$\sigma_{R_W^{\mu\nu}}(t, \boldsymbol{k}, 0) = \frac{B_{R_W^{\mu\nu}}}{|E_\gamma - M_{\bar{q}q}^{\text{PS}}|} \exp\{(E_\gamma - M_{\bar{q}q}^{\text{PS}})(T/2 - t)\}$$
$$+ \dots, \qquad (27)$$

where $B_{R_W^{\mu\nu}}$ is a prefactor and the ellipsis indicate terms that are subleading in the limit $T \to \infty$. For the D_s meson

$M_{\bar{q}q}^{\text{PS}} = M_{\eta_{ss'}} \sim 690$ MeV (see footnote 4 for the definition of $\eta_{ss'}$) so that the threshold value of $x_\gamma = x_\gamma^{\text{th}}$ at which the error on $R_W^{\mu\nu}(t, \boldsymbol{k}, 0)$ starts to grow asymptotically is given by $x_\gamma^{\text{th}} = 2 \frac{M_{\eta_{ss'}}}{M_{D_s}} \sim 0.7$, in agreement with our numerical results. Notice that in Eq. (27) $\sigma_{R_W^{\mu\nu}}(t, \boldsymbol{k}, 0)$ is finite only because of the finite temporal extent T of the lattice, and the signal-to-noise (S/N) ratio problem is thus amplified on large lattices. In addition, the S/N ratio problem becomes much more severe for heavy-light mesons with a u or d valence quark, such as $P = D$ or B mesons, where x_γ^{th} is proportional to the ratio between the pion mass and M_P. Large errors are therefore to be expected even for rather small values of x_γ. A way forward to mitigate this problem is briefly discussed at the end of Appendix A. We note that the approach that we propose in Appendix. A to tame the S/N ratio problem in Eq. (27) has been discussed in great detail in Ref. [17] where it was called the $3d$ method. In Ref. [17] the authors provide a detailed comparison, on a
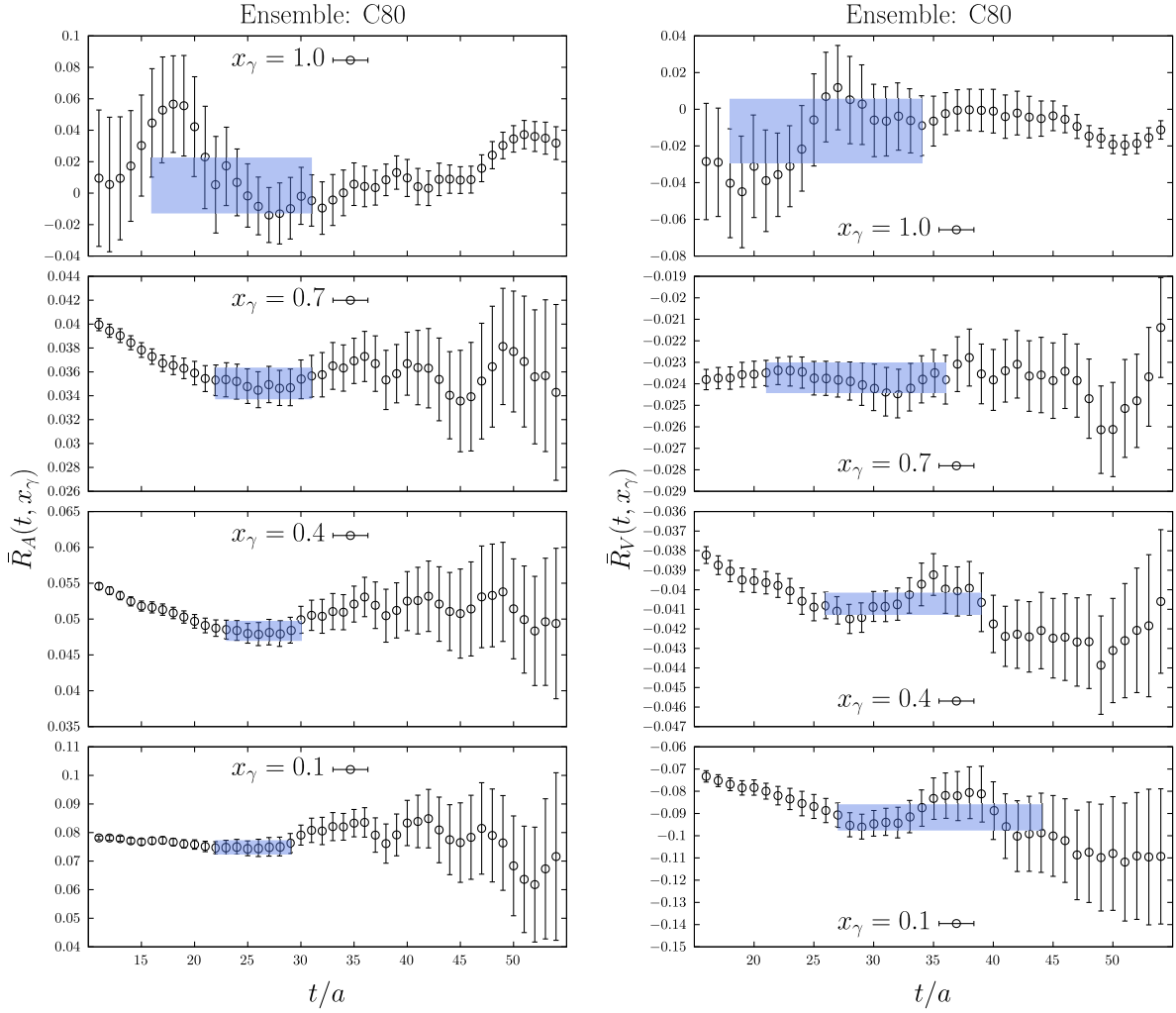
FIG. 4. The estimators $\bar{R}_A(t, x_\gamma)$ and $\bar{R}_V(t, x_\gamma)$ as a function of t/a for selected values of x_γ on the ensemble C80. In each figure the blue band corresponds to the result of a constant fit over the indicated region.

single coarse ensemble with $a \simeq 0.11$ fm, $T/a = 64$, and $M_\pi \simeq 340$ MeV, of the unwanted exponential contamination appearing in the $3d$ method and in the approach we use in the present work, based on the study of the three-point correlation function in Eq. (8) (in Ref. [17] this approach goes by the name of the $4d$ method). On the single ensemble analyzed, the authors of Ref. [17] find that the $3d$ method gives a better control over the unwanted exponentials. Here, we argue that the $3d$ method can also be helpful to tame the exponential S/N ratio problem for $E_\gamma > M_{\bar{q}q}^{\mathrm{PS}}$.

The ensembles of Table I all correspond to lattices with a spatial extent in the range $L \simeq 4.4$–5.4 fm. While these volumes are expected to be large enough for the finite-size effects (FSEs) on F_V and F_A to be small,[6] in order to estimate the residual FSEs, we have also used a fifth

ensemble, the cB211.072.96 ensemble (B96 for short), with the same parameters as the B64 ensemble, except that L is a factor $3/2$ larger. We have measured both F_V and F_A on the B96 ensemble up to $x_\gamma = 0.7$ using 100 gauge configurations.[7] As a conservative estimate of the FSEs, we associate to the values of $F_W(x_\gamma)$ determined on each of the ensembles of Table I an additional systematic uncertainty $\sigma_W^{\mathrm{FSE}}(x_\gamma)$ given by[8]

$$\frac{\sigma_W^{\mathrm{FSE}}(x_\gamma)}{F_W(x_\gamma)} = \left| \frac{\Delta F_W^L(x_\gamma)}{F_W(x_\gamma, \mathrm{B64})} \right| \mathrm{erf}\left(\frac{\Delta F_W^L(x_\gamma)}{\sqrt{2}\sigma_W^{\mathrm{comb}}(x_\gamma)} \right), \quad (28)$$

---

[6]In the electroquenched approximation employed in our computation, FSEs are expected to be exponentially suppressed by the spatial size of the lattice.

[7]Beyond $x_\gamma = x_\gamma^{\mathrm{th}} = 0.7$ the statistical errors on the B96 ensemble are too big for the results to be useful. Indeed, since on the B96 ensemble $T/a = 192$, the exponential increase of the error with the photon energy E_γ described by Eq. (27), is much faster than the one present on the B64 ensemble.

[8]For $x_\gamma \geq 0.8$ we associate the same relative systematic uncertainty as determined for $x_\gamma = 0.7$.
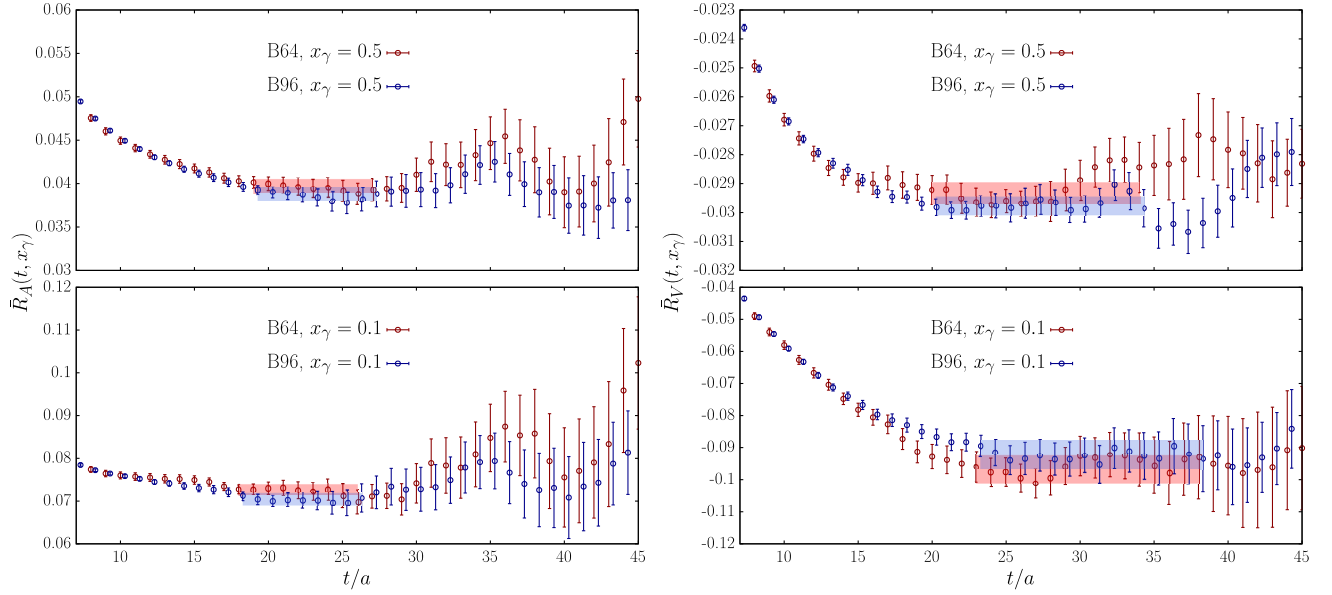
FIG. 5.   Comparison between the estimators $\bar{R}_A(t,x_\gamma)$ (left panels) and $\bar{R}_V(t,x_\gamma)$ (right panels) as determined on the B64 (red) and B96 (blue) ensembles, for two selected values of the dimensionless variable $x_\gamma = 0.1$ and 0.5. In each of the four figures the colored bands correspond to the result of a constant fit in the given time interval. The B96 data have been slightly shifted in time for visualization purposes.

where the subscript W represents V or A and

$$\Delta F^L_W(x_\gamma) \equiv |F_W(x_\gamma,\text{B96}) - F_W(x_\gamma,\text{B64})|,$$
$$\sigma^{\text{comb}}_W(x_\gamma) \equiv \sqrt{\sigma^{2,\text{stat}}_W(x_\gamma,\text{B64}) + \sigma^{2,\text{stat}}_W(x_\gamma,\text{B96})}, \quad (29)$$

which is the relative spread between the results obtained on the B96 and B64 ensembles, weighted by the probability that the spread is not due to a statistical fluctuation. In Fig. (5) we compare the two estimators $\bar{R}_A(x_\gamma)$ and $\bar{R}_V(x_\gamma)$, at two selected kinematic points $x_\gamma = 0.1$ and 0.5, determined on the B64 and B96 ensembles. Reassuringly, we find that for all values of x_γ and for both form factors $\sigma^{\text{FSE}}_W(x_\gamma)$ is smaller or of a similar size than the corresponding statistical uncertainty, and the difference between the results on the two volumes are most probably largely due to statistical fluctuations.

Next we consider cutoff effects. For each value of x_γ the extrapolation to the continuum limit is performed using the following Ansatz

$$F_W(x_\gamma,a) = F_W(x_\gamma)(1 + D_W(x_\gamma)(a\Lambda)^2 + D_{2,W}(x_\gamma)(a\Lambda)^4),$$
$$W = \{V,A\}, \quad (30)$$

with the parameter Λ chosen to be $\Lambda = M_{D_s} = 1.968$ GeV[9] and $F_W(x_\gamma)$, $D_W(x_\gamma)$ and $D_{2,W}(x_\gamma)$ are dimensionless fit parameters which depend on x_γ and are different

---

[9]With such a choice we find that the $D_W(x_\gamma)$ are of $O(1)$ (see Table IV).

for the two channels $W = \{V,A\}$. The result of the extrapolation for F_A and F_V, obtained using the Ansatz in Eq. (30) with the fit parameter D_2 fixed to zero, are shown in Figs. 6 and 7. In the two figures, the blue bands correspond to the linear a^2 extrapolation, performed omitting the measurement at the coarsest value of the lattice spacing. In Table IV, we report the values of the parameters $D_W(x_\gamma)$ obtained from the linear a^2 fit to the full dataset (orange band in Figs. 6 and 7), along with the corresponding reduced χ^2, which is always very good, except for F_A at the largest two values of x_γ ($x_\gamma = 0.9$ and 1.0). For most values of x_γ, the fit parameter D_W turns out to be of order

TABLE IV.   Values of the fit parameters $D_W(x_\gamma)$, their uncertainties ΔD_W, and the reduced χ^2 obtained in the linear fits to F_A and F_V for the ten values of x_γ considered in this work.

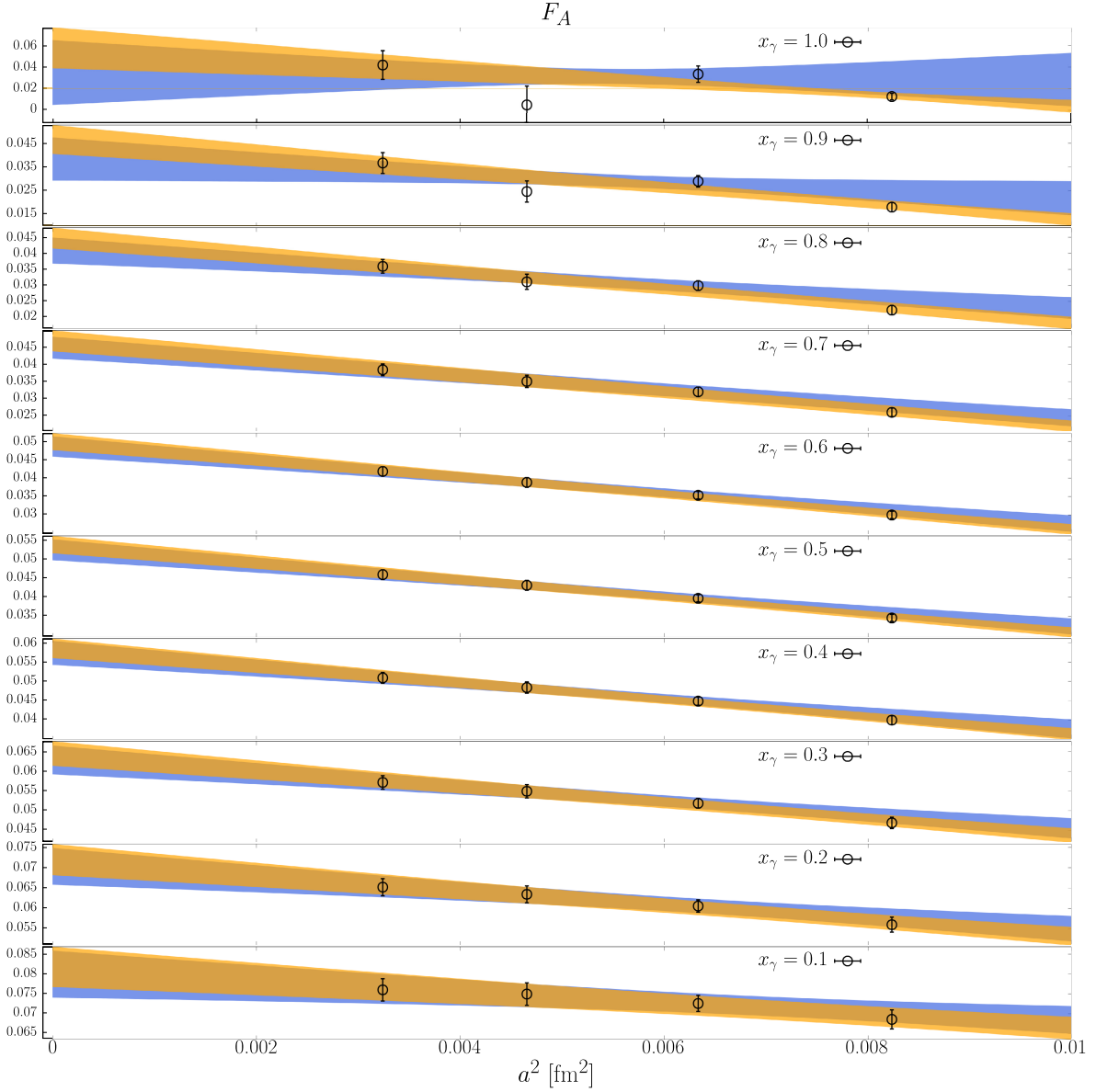|	F_A			F_V		
x_γ	D_A	ΔD_A	$\chi^2/\text{d.o.f.}$	D_V	ΔD_V	$\chi^2/\text{d.o.f.}$
0.1	-0.189	0.063	0.070	-0.197	0.132	0.656
0.2	-0.262	0.057	0.105	-0.339	0.038	0.786
0.3	-0.325	0.049	0.147	-0.414	0.024	0.396
0.4	-0.382	0.045	0.123	-0.470	0.019	0.089
0.5	-0.430	0.040	0.179	-0.517	0.017	0.488
0.6	-0.480	0.041	0.158	-0.551	0.016	1.597
0.7	-0.531	0.041	0.174	-0.595	0.018	0.946
0.8	-0.594	0.055	0.750	-0.676	0.030	0.510
0.9	-0.726	0.079	1.927	-0.824	0.063	0.756
1.0	-0.940	0.122	2.023	-0.964	0.123	0.241

FIG. 6. The extrapolation of F_A to the continuum limit for all ten values of x_γ considered in this work. The orange and blue bands correspond respectively to the extrapolation curves obtained including or excluding the data at the coarsest lattice spacing.

$\mathcal{O}(1)$, suggesting the presence of cutoff effects in F_V and F_A that are of order $\mathcal{O}(a^2 M_{D_s}^2)$.

We find that including the $D_{2,W}(x_\gamma)(a\Lambda)^4$ terms leads to overfitting without substantially improving the quality of the fit. The continuum values obtained using the Ansatz of Eq. (30) are always consistent within errors with those obtained from linear fits (i.e. with $D_{2,W}(x_\gamma)$ set to 0) shown in Figs. 6 and 7, but have substantially larger statistical uncertainties. Moreover, the coefficient $D_{2,W}(x_\gamma)$ turns out to be always consistent with zero within 1–1.5 standard deviations, a clear signal of overfitting. Given these observations we have decided to estimate the systematic uncertainty due to the continuum extrapolation, using the two linear extrapolations shown in each of Figs. 6 and 7.

Let f_A and f_B represent generically the continuum values of $F_A(x_\gamma)$ or $F_V(x_\gamma)$ at some value of x_γ obtained respectively from the linear fit by including or omitting the result at the coarsest lattice spacing. We determine the final central value $\bar{f}$ through a weighted average of the form

$$\bar{f} = w_A f_A + w_B f_B, \qquad w_A + w_B = 1. \quad (31)$$

Our estimate of the systematic error, which is added in quadrature to the combined statistical and finite-volume uncertainty, is then obtained using

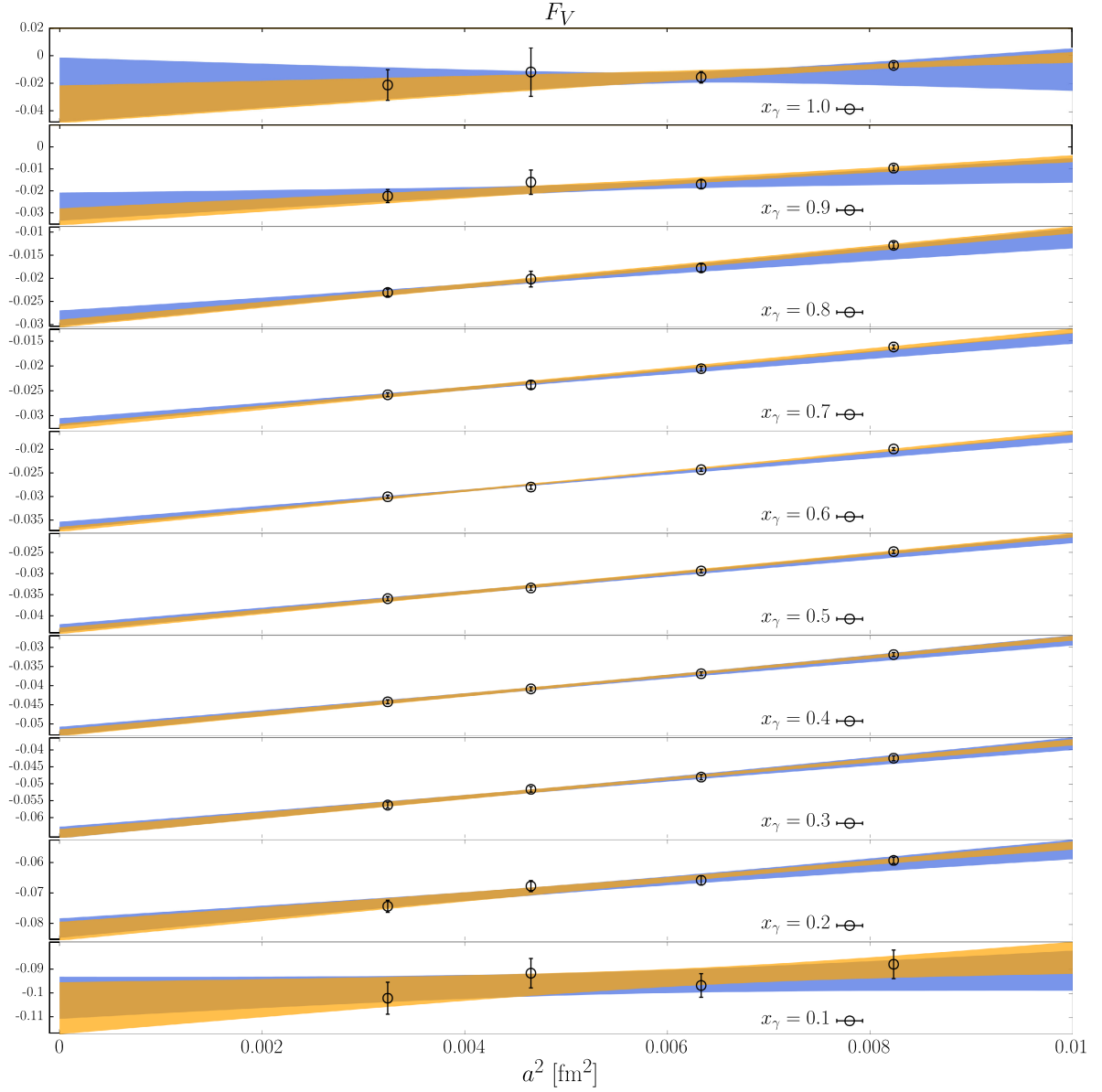$$\sigma_{\text{syst}}^2 = \sum_{i=A,B} w_i (f_i - \bar{f})^2. \quad (32)$$

FIG. 7.   The extrapolation of F_V to the continuum limit for all ten values of x_γ considered in this work. The orange and blue bands correspond respectively to the extrapolation curves obtained including or excluding the data at the coarsest lattice spacing.

The weights w_i, with $i = \{A, B\}$, are chosen according to the Akaike information criterion [41] (AIC) proposed in Ref. [42], namely

$$w_i \propto e^{-(\chi_i^2 + 2N_{\text{pars}}^{(i)} - 2N_{\text{data}}^{(i)})/2}, \tag{33}$$

where χ_i^2 is the total χ^2 obtained in the ith fit, and $N_{\text{pars}}^{(i)}$ and $N_{\text{meas}}^{(i)}$ are the corresponding number of fit parameters and measurements.[10]

---

[10]We have checked that the use of uniform weights, $w_A = w_B = 1/2$, leads to very similar results.

In Fig. 8 we show our final determination of the axial and vector form factors as a function of x_γ. The error bars include all the systematic uncertainties discussed above. The results for F_A and F_V are compared with those of Ref. [11], in which only the phase space region up to $x_\gamma \simeq 0.4$ had been explored. As the figures show, our results are in good agreement with those of Ref. [11] for both F_A and F_V, while the statistical uncertainty of the results is significantly improved, particularly for F_V. In Table V we collect our final results for the continuum values of F_A and F_V, while in Appendix B we present the full correlation matrix between the form factors evaluated at different values of x_γ, which may be useful for phenomenological analyses.
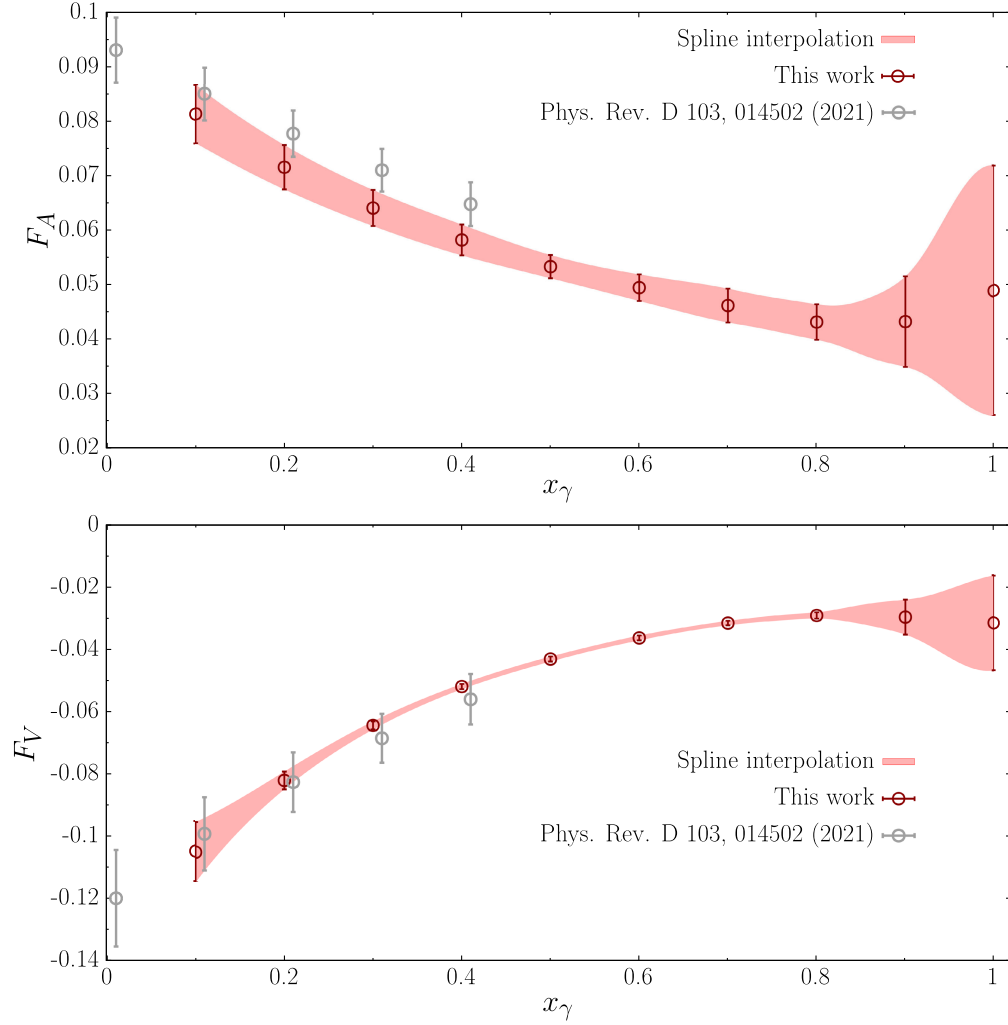
FIG. 8.   The form factors F_A (top figure) and F_V (bottom figure), obtained after the extrapolation to the continuum limit, shown as a function of the dimensionless variable x_γ. In each of the two figures, the red band is the result of a smooth cubic spline interpolation to our data. The gray data points correspond to the results from Ref. [11] which have been slightly shifted horizontally to facilitate comparison.

We have also determined separately the contributions to the form factors $F_{A,V}$ from the emission of the photon from the strange quark or the charm quark. In practice, the strange-quark (charm-quark) contribution to $R_{A,V}(t,\boldsymbol{k})$, indicated in the following by $R_{A,V}^{(s)}(t,\boldsymbol{k})$ $(R_{A,V}^{(c)}(t,\boldsymbol{k}))$, is obtained by setting the electric charge $q_c = 0$ ($q_s = 0$) in the evaluation of $C^{\mu\nu}(t,E_\gamma,\boldsymbol{k},\boldsymbol{p})$ in Eq. (8). The estimators $\bar{R}_{V,A}^{(s)}(t,x_\gamma)$ and $\bar{R}_{V,A}^{(c)}(t,x_\gamma)$ are obtained using the usual ratio of RCs Z_A/Z_V of Table III and the factor $\bar{Z}_V(t)$ of Eq. (21) so that

$$R_A(t,\boldsymbol{k}) = R_A^{(s)}(t,\boldsymbol{k}) + R_A^{(c)}(t,\boldsymbol{k}),$$

$$R_V(t,\boldsymbol{k}) = R_V^{(s)}(t,\boldsymbol{k}) + R_V^{(c)}(t,\boldsymbol{k}). \tag{34}$$

In Fig. 9 we show the strange- and charm-quark contributions to F_A and F_V, obtained after extrapolating the results

TABLE V.   Continuum results for F_A and F_V for the ten values of x_γ considered in this work. ΔF_A and ΔF_V are the final errors, which include all systematic uncertainties. The correlations between the form factors at different values of x_γ are given in Appendix B.

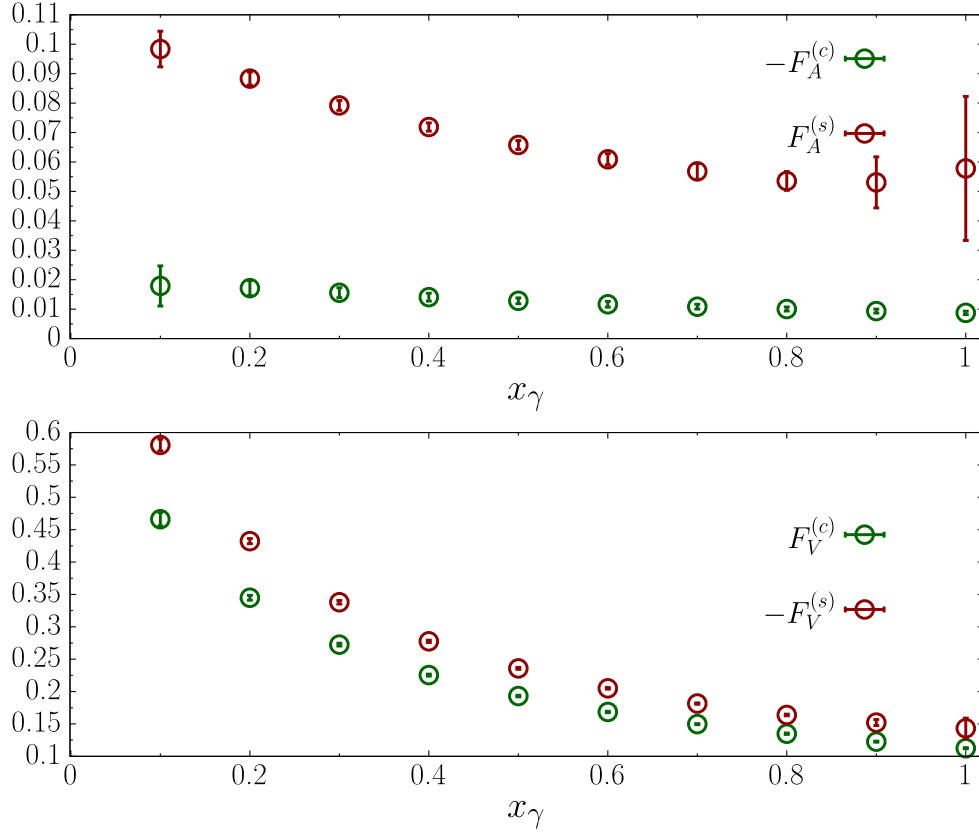| x_γ	F_A	ΔF_A	F_V	ΔF_V
0.1	0.0813	0.0054	−0.1048	0.0097
0.2	0.0715	0.0041	−0.0819	0.0028
0.3	0.0641	0.0033	−0.0643	0.0013
0.4	0.0582	0.0028	−0.0519	0.0008
0.5	0.0534	0.0021	−0.0431	0.0008
0.6	0.0495	0.0024	−0.0363	0.0008
0.7	0.0463	0.0031	−0.0316	0.0007
0.8	0.0432	0.0032	−0.0291	0.0010
0.9	0.0433	0.0083	−0.0297	0.0056
1.0	0.0489	0.0229	−0.0315	0.0152

FIG. 9.   The strange- and charm-quark contributions to F_A (top figure) and F_V (bottom figure) as a function of the dimensionless variable x_γ.

to the continuum limit following the same procedure as for the sum. It is interesting to note that while F_A it is completely dominated by the strange-quark contribution, there is a very significant cancellation between the strange and charm contributions to the vector form factor F_V. The cancellation between the two contributions becomes more pronounced at large values of x_γ. The implications of this cancellation in the vector form factor will be discussed in the next section. Finally, as is clear from Fig. 9, at large values of x_γ only the errors on $\bar{R}_{V,A}^{(s)}(t, x_\gamma)$ increase exponentially, while no degradation of the signal is present for $\bar{R}_{V/A}^{(c)}(t, x_\gamma)$, as expected from the analysis presented in Appendix A.

B. Differential decay rate and branching fraction

From the knowledge of the SD form factors F_V and F_A, the differential decay rate $d\Gamma(D_s \to \ell\nu\gamma)/dx_\gamma$ can readily be evaluated. The relevant formulae have been derived e.g. in Eqs. (1)–(31) of Ref. [12], to which we refer the reader for a more detailed discussion. However, for the sake of completeness we briefly summarize them here. The differential decay rate is expressed as a sum of three different contributions:

$$\frac{d\Gamma(D_s \to \ell\nu\gamma)}{dx_\gamma} = \frac{\alpha_{\rm em}}{4\pi}\Gamma^{(0)}\left\{\frac{dR^{\rm pt}}{dx_\gamma} + \frac{dR^{\rm int}}{dx_\gamma} + \frac{dR^{\rm SD}}{dx_\gamma}\right\}, \quad (35)$$

where $\Gamma^{(0)}$ is the leptonic decay rate in the absence of electromagnetism and is given explicitly by

$$\Gamma^{(0)} = \frac{G_F^2|V_{cs}|^2 f_{D_s}^2}{8\pi}M_{D_s}^3 r_\ell^2(1 - r_\ell^2)^2, \quad (36)$$

and the three quantities $dR^{\rm pt}/dx_\gamma$, $dR^{\rm int}/dx_\gamma$, and $dR^{\rm SD}/dx_\gamma$ correspond respectively to the pointlike, interference, and SD contribution. The pointlike contribution does not depend on the SD form factors, while the interference and the SD contribution depend on F_V and F_A linearly and quadratically, respectively. The explicit expression of the three terms is the following ($r_\ell \equiv m_\ell/M_{D_s}$):

$$\frac{dR^{\rm pt}}{dx_\gamma} = -\frac{2}{(1 - r_\ell^2)^2}\frac{1}{x_\gamma}\left\{\left[\frac{(2 - x_\gamma)^2}{1 - x_\gamma} - 4r_\ell^2\right](1 - x_\gamma - r_\ell^2)\right.$$
$$\left. - [2(1 - r_\ell^2)(1 + r_\ell^2 - x_\gamma) + x_\gamma^2]\log\left(\frac{1 - x_\gamma}{r_\ell^2}\right)\right\},$$
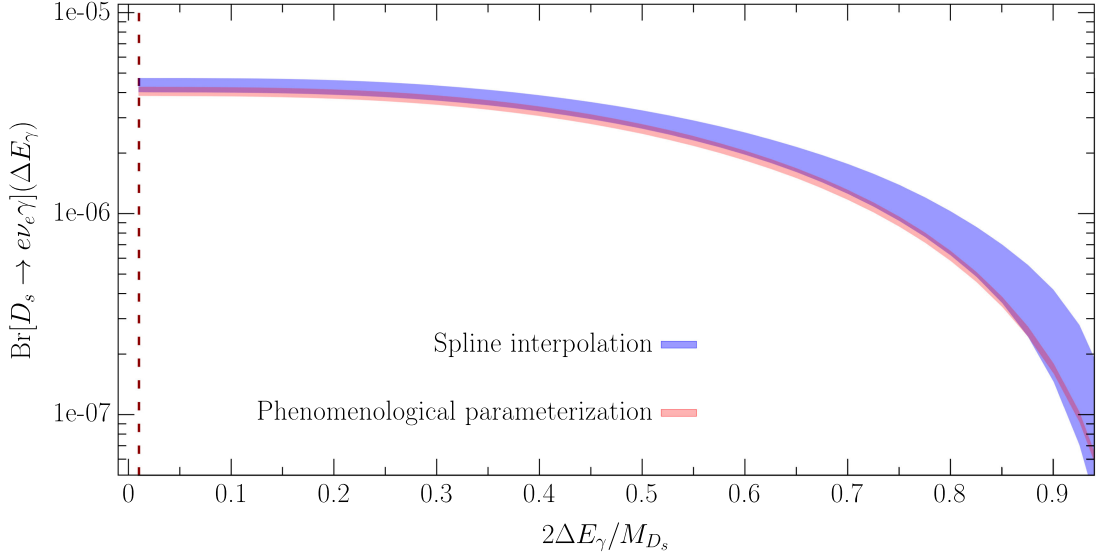$$(37)$$

FIG. 10. The branching fraction $\mathrm{Br}[D_s \to e\nu_e\gamma](\Delta E_\gamma)$ for different values of the lower cutoff ΔE_γ on the photon energy. The red vertical dashed line represents the experimental cut-off $\Delta E_\gamma = 10$ MeV imposed in the BESIII experiment. The blue and red bands correspond respectively to the branching fraction as obtained by employing the spline interpolation of the lattice results for the form factors or their phenomenological parametrization obtained by fitting the Ansatz of Eq. (43) (see also Sec. V and Table VI for more details).

$$\frac{dR^{\mathrm{int}}}{dx_\gamma} = -\frac{2M_{D_s}}{f_{D_s}(1-r_\ell^2)^2}\left\{F_A x_\gamma\left[\frac{r_\ell^4}{1-x_\gamma} - 1 + x_\gamma + 2r_\ell^2\log\left(\frac{1-x_\gamma}{r_\ell^2}\right)\right] + (F_V - F_A)x_\gamma^2\left[\frac{r_\ell^2}{1-x_\gamma} - 1 + \log\left(\frac{1-x_\gamma}{r_\ell^2}\right)\right]\right\}, \quad (38)$$

$$\frac{dR^{\mathrm{SD}}}{dx_\gamma} = \frac{M_{D_s}^2}{f_{D_s}^2}(F_V^2 + F_A^2)\frac{x_\gamma^3}{r_\ell^2(1-r_\ell^2)^2}$$
$$\times \frac{(2 + r_\ell^2 - 2x_\gamma)(1 - x_\gamma - r_\ell^2)^2}{6(1-x_\gamma)^2}. \quad (39)$$

The total decay rate

$$\Gamma_\ell(\Delta E_\gamma) \equiv \int_{\frac{2\Delta E_\gamma}{M_{D_s}}}^{1-r_\ell^2} dx_\gamma \frac{d\Gamma(D_s \to \ell\nu\gamma)}{dx_\gamma} \quad (40)$$

can be then evaluated for any desired photon energy cut ΔE_γ using the previous formulas and our determination of the form factors F_V and F_A. As Eqs. (37)–(39) indicate, the pointlike contribution gives rise, in the soft photon limit $\Delta E_\gamma \to 0$, to a logarithmically divergent contribution proportional to $\log(\Delta E_\gamma)$ and is therefore the dominant contribution in $\Gamma_\ell(\Delta E_\gamma)$ for sufficiently small values of ΔE_γ.[11] However, the pointlike contribution is also chirally suppressed with respect to the SD contribution by the factor

---

[11]The infrared divergence in the leptonic decay with a real photon in the final state is canceled by the $\mathcal{O}(\alpha_{\mathrm{em}})$ virtual photon contribution to the purely leptonic decay amplitude, through the Bloch-Nordsieck mechanism [43]. The inclusive leptonic decay rate $P \to \ell\nu(\gamma)$ is infrared finite.

$r_\ell^2 = (m_\ell/M_{D_s})^2$. Unlike the pointlike contribution, the SD contribution to $d\Gamma(D_s \to \ell\nu\gamma)/dx_\gamma$ is small at small photon energies, then grows reaching a maximum at some value of the photon energy which depends on the specific channel considered, and then decreases to zero at the edge of phase space, i.e. for $x_\gamma = 1 - r_\ell^2$. Therefore, for a sufficiently large photon energy cutoff ΔE_γ and a small value of r_ℓ, the SD contribution to $\Gamma_\ell(\Delta E_\gamma)$ is the dominant one.

For the radiative leptonic decays of the D_s meson, the only experimental measurement that is currently available is the branching fraction for $D_s \to e\nu_e\gamma$, for which the BESIII Collaboration has given the upper bound at 90% confidence level [8]

$$\mathrm{Br}[D_s \to e\nu_e\gamma](\Delta E_\gamma) \equiv \frac{\Gamma_e(\Delta E_\gamma)}{\Gamma_{\mathrm{tot}}} < 1.3 \times 10^{-4},$$
$$\Gamma_{\mathrm{tot}}^{-1} = (5.04 \pm 0.04) \times 10^{-13} \text{ s} \quad [37],$$
$$(41)$$

including photons with energies $E_\gamma > \Delta E_\gamma = 10$ MeV. Because of the small mass of the electron, $r_e \simeq 2.6 \times 10^{-4}$ compared to $r_\mu \simeq 5.4 \times 10^{-2}$ and $r_\tau \simeq 0.9$, the electron channel is the most sensitive to the vector and axial form factors F_V and F_A and is therefore the most interesting one phenomenologically. In Fig. 10 we show

our determination of the branching fraction as a function of the cutoff on the photon energy, starting from the cut $\Delta E_\gamma = 10$ MeV employed by the BESIII Collaboration in Ref. [8], which is indicated in the figure by the dashed red line. For this calculation, we used the following values of the Cabibbo-Kobayashi-Maskawa (CKM) matrix element V_{cs} and of the D_s decay constant, which we have taken from the 2021 FLAG review [44]

$$|V_{cs}| = 0.9741(65), \qquad f_{D_s} = 249.9(0.5) \text{ MeV}$$
$$[N_f = 2 + 1 + 1 \text{ averages}]. \tag{42}$$

We have computed the branching fraction by using the form factors $F_{A,V}$ determined either from the spline interpolation of our numerical lattice results or by fitting to the phenomenological parametrization of the form factors given in Eq. (43) below and discussed in the next section. The two different determinations of the branching fraction are represented in Fig. 10 by the blue and red bands respectively. The phenomenological parametrization of the form factor leads to a much more precise determination of the form factors in the kinematical region of high values of x_γ than the spline interpolation of the lattice data. This is due to the fact that the fit parameters are mainly determined from the most statistically accurate data points, which are the ones at low and intermediate values of x_γ, while the spline interpolation is designed to always reproduce the actual data points with their corresponding error range. As a consequence, the branching fraction obtained through the phenomenological parametrization of the form factors is more precise than the one obtained by using the spline interpolation, and the difference in the precision increases

as the lower cutoff on the photon energy ΔE_γ increases. On the other hand, results obtained by using the spline interpolation of the lattice data are less affected by potential systematic effects due to model dependence and for this reason we conservatively consider these as our final results. Note however, that the two determinations of the branching fraction are always compatible within errors.

From Fig. 10 we see that the results obtained for $\text{Br}[D_s \to e\nu_e\gamma](10 \text{ MeV})$ using either the spline interpolation $(\text{Br}[D_s \to e\nu_e\gamma](10 \text{ MeV}) = 4.4(3) \times 10^{-6})$ or the phenomenological parametrization of the form factors $(\text{Br}[D_s \to e\nu_e\gamma](10 \text{ MeV}) = 4.1(2) \times 10^{-6})$ are well within the upper bound at 90% confidence level set by the BESIII Collaboration $(\text{Br}[D_s \to e\nu_e\gamma](10 \text{ MeV}) < 1.3 \times 10^{-4})$. Moreover, they are also much smaller than the quark-model predictions of Refs. [45,46] which estimate a branching fraction of order 10^{-5}–10^{-4}, and of the determination of Ref. [18] where a branching fraction of order 10^{-3} is obtained combining perturbative QCD with the heavy-quark effective theory. We find that, already for $\Delta E_\gamma = 10$ MeV and even more so for higher-energy cuts, the decay rate is completely dominated by the SD term. The pointlike contribution is always below one percent and the interference contribution is even smaller. For comparison, adopting the same cut on the photon energy $(\Delta E_\gamma = 10 \text{ MeV})$, the corresponding branchings into muon or τ are respectively $1.86(3) \times 10^{-4}$ and $1.20(2) \times 10^{-6}$, and in both cases are dominated by the pointlike contribution. Finally, in Fig. 11 we provide our determination of the SD contribution to the differential branching fraction in the electron channel, which has a maximum for a value of x_γ of about 0.6–0.7. The blue and
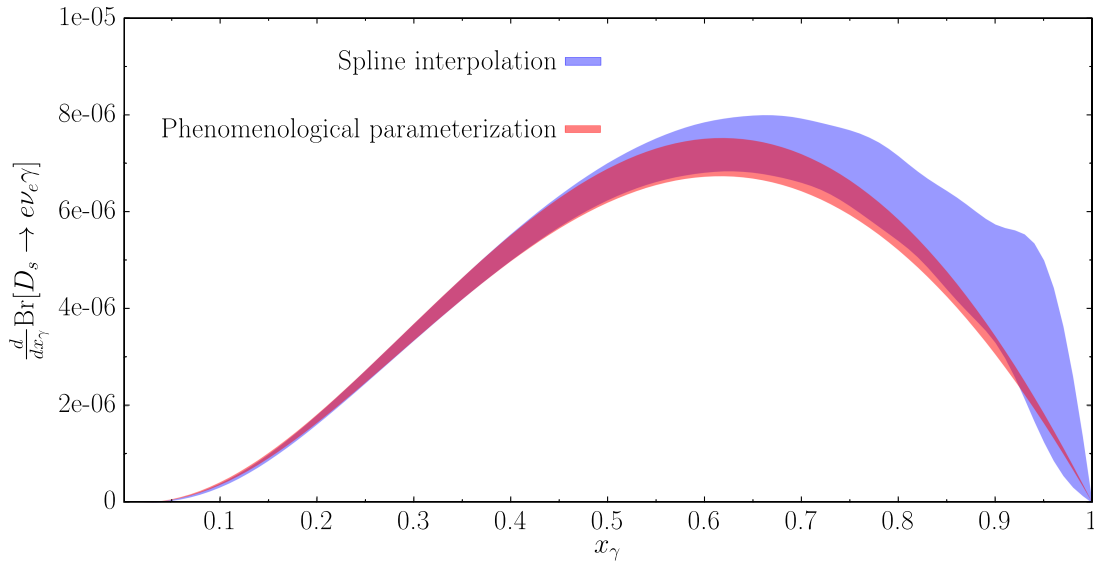

FIG. 11. The SD contribution to the differential branching fraction for the decay $D_s \to e\nu_e\gamma$ as a function of x_γ. The blue and red bands correspond respectively to the decay rate obtained by employing the spline interpolation of the lattice results for the form factors or their phenomenological parametrization obtained by fitting the Ansatz of Eq. (43) (see also Sec. V and Table VI for more details).

TABLE VI. Values of the parameters C_W, R_W and B_W for the two form factors F_A and F_V, and for the individual contributions $F_{A,V}^{(c)}$ and $F_{A,V}^{(s)}$, obtained by fitting the Ansatz of Eq. (43). For the axial data, and for the total vector form factor, the parameter B_W is not included in the fit and has been set to zero, since it is not necessary to describe the data. Correlations among the fitted parameters are also reported in this table.

	C_W	R_W	B_W	cor(C_W, R_W)	cor(C_W, B_W)	cor(R_W, B_W)	χ^2/d.o.f.
F_A	0.0518(30)	1.413(30)	0 (fixed)	0.766	$\cdots$	$\cdots$	0.41
$F_A^{(c)}$	$-0.0135(10)$	1.453(59)	0 (fixed)	-0.732	$\cdots$	$\cdots$	0.23
$F_A^{(s)}$	0.0662(56)	1.423(36)	0 (fixed)	0.975	$\cdots$	$\cdots$	0.24
F_V	$-0.01792(76)$	1.091(11)	0 (fixed)	-0.936	$\cdots$	$\cdots$	0.45
$F_V^{(c)}$	0.0624(15)	1.0809(43)	0.0369(14)	0.922	-0.864	-0.819	0.31
$F_V^{(s)}$	$-0.0792(24)$	1.0794(37)	$-0.0367(31)$	-0.911	-0.936	0.831	1.8

red bands in Fig. 11 represent respectively the results obtained by using the spline interpolation of the lattice results for the form factors or the phenomenological parametrization based on their fit to the Ansatz of Eq. (43) below. As before, in the region of high values of x_γ the results based on the phenomenological parametrization of the form factors become much more precise than the ones based on their spline interpolation. However, the two determinations are always compatible within errors. Additional branching fractions, with specific cuts on the photon and/or lepton energies, are available on request from the authors.

V. PHENOMENOLOGICAL PARAMETRIZATION OF THE FORM FACTORS

In this section we present a parametrization of the form factors inspired by single-pole dominance. In this approximation the form factor is described in terms of the propagation of the nearest resonance. We find that a good description of the momentum dependence of our lattice data is obtained by employing the following Ansatz:

$$F_W(x_\gamma) = \frac{C_W}{\sqrt{R_W^2 + \frac{x_\gamma^2}{4}}\left(\sqrt{R_W^2 + \frac{x_\gamma^2}{4}} + \frac{x_\gamma}{2} - 1\right)} + B_W,$$
$$W = \{A, V\}, \tag{43}$$

in which the single-pole dominance approximation corresponds to fixing $R_W = M'/M_{D_s}$ where M' is the mass of the nearest resonance, and setting $B_W = 0$. Here instead C_W, R_W and B_W are three free parameters to be determined from the fit. The constant term B_W represents the leading, nonsingular correction in the Laurent expansion of a function around a pole. We refer the reader to Appendix C for a more detailed analysis of the different Ansätze which we have examined.

The Ansatz of Eq. (43) has also been used to fit separately the contributions from the emission of the photon from the charm and strange valence quarks.

These are simply obtained by setting the charge of the other quark to zero. We label these separate contributions by $F_{A,V}^{(c)}$ and $F_{A,V}^{(s)}$, where the superscript indicates the quark from which the photon has been emitted. Interestingly, we find that including the parameter B_W is only required to obtain an acceptable fit for the separate contributions $F_V^{(c)}$ and $F_V^{(s)}$. For all the other cases [$F_A^{(c)}$, $F_A^{(s)}$, F_A, and F_V], B_W can be set to 0 without increasing the χ^2/d.o.f., resulting in good parametrizations of the form factors. The results of the fits are reported in Table VI, while in Fig. 12 we plot the resulting fitting functions together with our lattice data. We see from Fig. 12 and Table VI that the fits provide a very good representation of our lattice data and low values of the correlated χ^2, even for the most precisely determined form factors. The remarkably strong, $\mathcal{O}(90\%)$, cancellation between the obtained values of $B_V^{(c)}$ and $B_V^{(s)}$ in Table VI explains why B_V can be dropped when fitting the total vector form factor. The degree of cancellation between $B_V^{(c)}$ and $B_V^{(s)}$, and also between the contributions to the form factor F_V from $F_V^{(c)}$ and $F_V^{(s)}$ in the lower panel of Fig. 9, depends on both the charges and masses of the two valence quarks and should therefore be considered to be accidental. It will be interesting in the future to observe to what extent these cancellations hold for the decays of the B-meson. Finally, we observe that the parametrization we provide for the form factors is more precise than the lattice data points for kinematics above the threshold value $x_\gamma \simeq 0.8$. This is because the fit parameters are mainly determined from the most statistically accurate data points, which are the ones at low and intermediate values of x_γ.

Single-pole dominance implies that the values of R_W and C_W are related, respectively, to the masses of the nearest internal resonances contributing to the correlator and to their transition amplitudes to the external states. In the present case, the resonances are the D_s^* for the vector channel and the D_{s1} for the axial one. The values of the amplitudes C_W are therefore related to the couplings $g_{D_s^* D_s \gamma}$ and $g_{D_{s1} D_s \gamma}$, i.e. to the $D_s^* \to D_s \gamma$ and $D_{s1} \to D_s \gamma$ decay
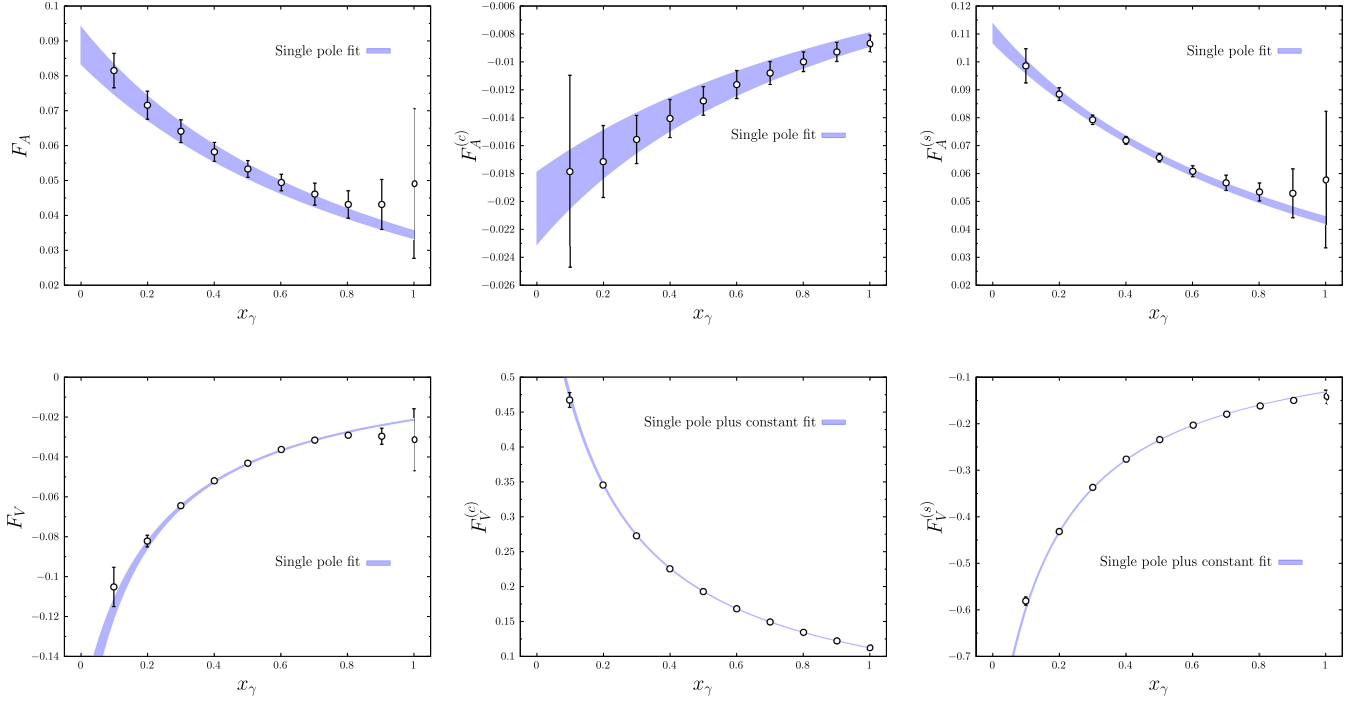
FIG. 12. The fit functions corresponding to the Ansatz of Eq. (43) are plotted, along with the lattice data, for the axial channel (top panels) and for the vector channel (bottom panels). The "single-pole fit" denotes the fit to the data with B_W fixed to zero, while "Single pole plus constant fit" denotes the fit to the data with all the three parameters C_W, R_W and B_W left free.

amplitudes respectively. However, for such an interpretation of the C_W to be considered to be physically meaningful, we first need to check that the fitted values are stable under variations of the fit Ansatz. We perform such an analysis in detail in Appendix C. The outcome is that the data in the axial channel, i.e. for F_A, $F_A^{(c)}$ and $F_A^{(s)}$, are well described by any of the different Ansätze we employed, but the resulting values for the amplitude C_A are very different depending on the Ansatz which was used. We conclude that the fitted value of C_A is not stable and is not reliable as an estimate of the coupling $g_{D_{s1}D_s\gamma}$. Note that in the axial channel, there is a second resonance, the $D_{s1}(2536)$, with a mass which is only 76 MeV above the nearest resonance, the $D_{s1}(2460)$. Since the difference in the masses is so small, the fitted residue C_A may encode contributions from both of these internal states, resulting in an unreliable determination of the coupling $g_{D_{s1}D_s\gamma}$. For the vector channel on the other hand, we found that the value of C_V is very stable under variations of the fit Ansatz, provided that the corresponding fits result in a low value of $\chi^2/\text{d.o.f.}$.

Having established in Appendix C that the value of C_V is stable, we obtain the corresponding value of the coupling $g_{D_s^*D_s\gamma}$, using the relation,

$$C_V = -\frac{M_{D_s^*} f_{D_s^*} g_{D_s^*D_s\gamma}}{2M_{Ds}}, \qquad (44)$$

where $f_{D_s^*}$ is the decay constant of the D_s^* meson, for which we take the value $f_{D_s^*} = 268.8(6.6)$ MeV obtained from the lattice computation of Ref. [47]. In Table VII, we report our estimate for the coupling $g_{D_s^*D_s\gamma}$, and for the individual contributions from the radiation from the strange and charm quarks. In the quoted uncertainties, we include an estimate of the systematic error due to the use of single-pole dominance as a model parametrization of the form factors. This is obtained in Appendix C from the variation of the results in Table IX determined using different Ansätze. In Table VII we also provide a comparison of our results with the values of the $g_{D_s^*D_s\gamma}$ couplings obtained from a direct

TABLE VII. Our results for the $g_{D_s^*D_s\gamma}$, $g_{D_s^*D_s\gamma}^{(s)}$ and $g_{D_s^*D_s\gamma}^{(c)}$ couplings are presented and compared to the previous computations of Refs. [21,22], based on lattice simulations and LCSR at NLO, respectively. Note the indirect nature of our estimate of the couplings, obtained by using an effective single-pole parametrization of the radiative form factors, as compared to the direct lattice computation of the $D_s^* \to D_s\gamma$ decay amplitude [21].

	LCSR [22]	HPQCD [21]	This paper
$g_{D_s^*D_s\gamma}$ [GeV^{-1}]	0.60(19)	0.10(2)	0.118(13)
$g_{D_s^*D_s\gamma}^{(s)}$ [GeV^{-1}]	1.0	0.50(3)	0.532(15)
$g_{D_s^*D_s\gamma}^{(c)}$ [GeV^{-1}]	-0.4	$-0.40(2)$	$-0.415(16)$
$\frac{g^{(s)}}{g^{(c)}}$	-2.5	$-1.25(10)$	$-1.282(61)$

lattice computation of the $D_s^* \to D_s \gamma$ decay amplitude [21], and from the calculation based on LCSR at next-to-leading order [22]. Our results are in excellent agreement with those of Ref. [21] and with the value of $g_{D_s^* D_s \gamma}^{(c)}$ obtained in the LCSR calculation [22]. However, we find a discrepancy of a factor of about 2 with the value of $g_{D_s^* D_s \gamma}^{(s)}$ obtained in Ref. [22] which, given the strong cancellation between the strange and charm-quark contributions, is amplified in the total coupling $g_{D_s^* D_s \gamma}$ to a factor of about 5; specifically the value from the LCSR calculation is about five times larger than the ones obtained from the lattice computations.[12]

The authors of Ref. [23] have also provided the values of the radiative form factors F_A and F_V for the D_s meson at a single kinematic point $x_\gamma = 0.846$; $F_A(x_\gamma = 0.846) = -0.44$ and $F_V(x_\gamma = 0.846) = -0.11$. They add that they refrain from estimating the uncertainties on these values as they "only aim to provide rough estimates in order to motivate experimental searches" [23]. Nevertheless, these estimates are in strong disagreement with the values collected in Table V from our direct lattice computation. In particular, we notice that, around this specific kinematic point, the magnitudes of F_V differ by approximately a factor 4, while for F_A the results differ by an order of magnitude and have the opposite sign. This raises some questions about the precision of the approach of Refs. [22,23], based on LCSR, for describing heavy-meson radiative form factors.

VI. CONCLUSIONS

In this paper we have presented a lattice calculation, in the electroquenched approximation, of the structure-dependent axial and vector form factors, F_A and F_V, which contribute to the amplitudes for the radiative leptonic decays $D_s \to \ell \nu_\ell \gamma$. Our results extend and improve the analysis presented in Ref. [11], and are the first lattice predictions for these form factors over the whole physical phase space in the continuum limit.

We have also presented the individual contributions to the form factors from the emission of the photon from the charm and strange valence quarks, $F_{V,A}^{(c)}$ and $F_{V,A}^{(s)}$ respectively, with $F_{V,A} = F_{V,A}^{(c)} + F_{V,A}^{(s)}$. A remarkable feature is that $F_V^{(c)}(x_\gamma) \approx -F_V^{(s)}(x_\gamma)$, see the lower panel of Fig. 9, so that there is a very significant cancellation in the determination of $F_V(x_\gamma)$. The axial form factor F_A is dominated by $F_A^{(s)}$ and there is no such cancellation, see the upper panel of Fig. 9.

We use our results for the form factors to compute the differential decay rate for the process $D_s \to e \nu_e \gamma$ as a

function of the photon energy in the meson rest frame, separating the SD contribution from the pointlike one. By integrating the differential decay rate, we obtain the branching ratio for the $D_s \to e \nu_e \gamma$ decay as a function of the lower cutoff, ΔE_γ, on the energy of the photon in the rest frame of the decaying meson. Our result for the branching ratio for $\Delta E_\gamma = 10$ MeV is $4.4(3) \times 10^{-6}$, well below the upper bound of 1.3×10^{-4} set by the BESIII Collaboration [8]. Even for as low a value of ΔE_γ as 10 MeV, we find that the SD contribution dominates the branching ratio due to the strong helicity suppression, by a factor $r_e^2 = (m_e/M_{D_s})^2$, of the pointlike term.

Having determined the form factors, we use the results to investigate the validity and applicability of model-dependent calculations, such as ones based on single-pole dominance or light cone sum rules. Such model estimates are commonly used in the analysis of radiative processes involving heavy mesons for which lattice calculations are often not available. We showed that the LCSR computations at next-to-leading order of Refs. [22,23] fail to reproduce our results for the form factors of the D_s meson, and that a pure VMD parametrization does not always reproduce their momentum behavior. In Eq. (43) and Table VI we propose a simple parametrization of the form factors, based on an extension of the single-pole dominance Ansatz, which reproduces our lattice results very well and may therefore be useful for future phenomenological analyses.

For $F_V(x_\gamma)$ we find that results for the residue of the pole are very stable, allowing us to interpret the result in terms of the $g_{D_s D_s^* \gamma}$ coupling. The result is presented in Table VII, where it is also compared to the results from a direct lattice computation of the rate for the decay $D^* \to D \gamma$ [21] (we find good agreement) and to the LCSR calculation of Ref. [22] (we disagree significantly).

A nonperturbative, model-independent theoretical prediction for the amplitudes of real photon emission in leptonic decays is important for testing the Standard Model and for searches for new physics. Indeed, such results are required in order to include $O(\alpha_{em})$ corrections in the determination of fundamental SM parameters such as the CKM matrix elements. In addition, the SD contribution to $P \to \ell \nu_\ell \gamma$ decays probes the internal structure of the decaying meson and by comparing SM results for the form factors to experimental measurements one can test for hypothetical new physics effects. This is especially true for the decays of heavy mesons into an electron and its neutrino, where the SD contribution dominates the rate already at low photon energies such as 10 MeV, which are included in some current experimental studies. First-principles lattice computations are particularly important for heavy mesons since chiral perturbation theory does not apply in that case. For this reason, in the future we plan to compute the radiative SD form factors also for the D and B mesons. When applying the strategy that we have presented

---

[12]According to Ref. [48] the uncertainty in the $g_{D_s^* D_s \gamma}$ coupling given in Ref. [22] may be an underestimate because of the significant cancellation between the charm- and the strange-quark contributions.

in this work to these mesons however, the presence of a light valence quark will significantly lower the threshold value of the photon energy above which statistical fluctuation start to grow exponentially. We have identified the origin of this issue in Appendix A, where we also briefly discuss a possible way to mitigate this problem based on the different lattice approach proposed in Ref. [17], where it is called the 3d method.

APPENDIX A: BEHAVIOR OF THE SIGNAL-TO-NOISE RATIO FOR F_V AND F_A AT LARGE x_γ

In this appendix, we show why the intrinsic statistical fluctuations of $C_W^{\mu\nu}(t, E_\gamma, \boldsymbol{k}, \boldsymbol{p})$ become exponentially large for small values of t and large values of x_γ. For this discussion we make a certain number of simplifications, but these have no impact on the main conclusions. We consider only the case $\boldsymbol{p} = 0$, i.e. we always work in the decaying hadron's reference frame. We shall also use continuum notation throughout this appendix, and replace lattice sums by definite integrals. Also, when considering the Euclidean three-point correlation function in Eq. (8) we only consider the term with $t_y < T/2$, which is the dominant one in the limit $T \to \infty$. We discuss the case of an arbitrary pseudoscalar meson $P = \bar{U}\gamma^5 D$ made of an up- and a down-type quark.

We choose the 4-momentum $k = (|\boldsymbol{k}|, \boldsymbol{k})$ and $p = (m_P, \boldsymbol{0})$, therefore we now denote the correlation function $C_W^{\mu\nu}(t; k, p)$ in Eq. (8) simply by $C_W^{\mu\nu}(t, \boldsymbol{k})$. For $t, t_y < T/2$ it is given by

$$C_W^{\mu\nu}(t; \boldsymbol{k}) = -i \int_0^{T/2} dt_y e^{E_\gamma t_y} \langle 0|\hat{T}[j_W^\nu(t, \boldsymbol{0})\hat{j}_{\text{em}}^\mu(t_y, \boldsymbol{k}) \\ \times \hat{\phi}_P^\dagger(0, \boldsymbol{0})]|0\rangle, \tag{A1}$$

where

$$\hat{\phi}_P^\dagger(t_x, \boldsymbol{p}) = \int d^3 x \phi_P^\dagger(t_x, \boldsymbol{x}) e^{i\boldsymbol{p}\cdot\boldsymbol{x}},$$

$$\hat{j}_{\text{em}}^\mu(t_y, \boldsymbol{k}) = \int d^3 y j_{\text{em}}^\mu(t_y, \boldsymbol{y}) e^{-i\boldsymbol{k}\cdot\boldsymbol{y}} \tag{A2}$$

and $E_\gamma = |\boldsymbol{k}|$. We now separate the contribution from the region with $t_y < t$ from that with $t_y > t$,

$$C_W^{\mu\nu}(t; \boldsymbol{k}) \equiv C_W^{\mu\nu;1}(t, \boldsymbol{k}) + C_W^{\mu\nu;2}(t, \boldsymbol{k})$$

$$= -i \int_0^t dt_y e^{E_\gamma t_y} \langle 0|j_W^\nu(t, \boldsymbol{0})\hat{j}_{\text{em}}^\mu(t_y, \boldsymbol{k})\hat{\phi}_P^\dagger(0, \boldsymbol{0})|0\rangle$$

$$- i \int_t^{T/2} dt_y e^{E_\gamma t_y} \langle 0|\hat{j}_{\text{em}}^\mu(t_y, \boldsymbol{k})j_W^\nu(t, \boldsymbol{0})\hat{\phi}_P^\dagger(0, \boldsymbol{0})]|0\rangle. \tag{A3}$$

The time ordering relevant for our discussion is $t < t_y < T/2$, i.e. with the weak current acting before the electromagnetic current; this corresponds to the second contribution to the correlation function, $C_W^{\mu\nu;2}(t, \boldsymbol{k})$. We also distinguish the contributions to $C_W^{\mu\nu;2}(t, \boldsymbol{k})$ from the emission of the real photon from the up-type (U) or down-type (D) valence quark, and define

$$C_W^{\mu\nu;2}(t, \boldsymbol{k}) \equiv C_{U,W}^{\mu\nu;2}(t, \boldsymbol{k}) + C_{D,W}^{\mu\nu;2}(t, \boldsymbol{k}), \tag{A4}$$

where

$$C_{f,W}^{\mu\nu;2}(t, \boldsymbol{k}) \equiv -i \int_t^{T/2} dt_y e^{E_\gamma t_y} \langle 0|\hat{j}_{f,\text{em}}^\mu(t_y, \boldsymbol{k})j_W^\nu(t, \boldsymbol{0}) \\ \times \hat{\phi}_P^\dagger(0, \boldsymbol{0})]|0\rangle, \qquad f = (U, D) \tag{A5}$$

in terms of the single-flavor contribution to the current,

$$\hat{j}_{f,\text{em}}^\mu(t_y, \boldsymbol{k}) \equiv q_f \int d^3 y e^{-i\boldsymbol{k}\cdot\boldsymbol{y}} \bar{\psi}_f(t_y, \boldsymbol{y})\gamma^\mu \psi_f(t_y, \boldsymbol{y}). \tag{A6}$$

Since we aim at understanding the behavior of the error at small t, we focus on the case in which the weak current j_W^ν and the interpolating operator ϕ are separated by a time distance of a few lattice spacings. In this case, we can interpret the quantity

$$O_W^\nu(t) \equiv j_W^\nu(t, \boldsymbol{0})\hat{\phi}_P^\dagger(0, \boldsymbol{0}) \tag{A7}$$

as a nonlocal interpolating operator for vector states (in both cases $W = V, A$), and

$$M_{f,W}^{\mu\nu}(t_y - t, t, \boldsymbol{k}) \equiv \langle 0|\hat{j}_{f,\text{em}}^\mu(t_y, \boldsymbol{k})j_W^\nu(t, \boldsymbol{0})\hat{\phi}_P^\dagger(0, \boldsymbol{0})|0\rangle$$

$$= \langle 0|\hat{j}_{f,\text{em}}^\mu(t_y, \boldsymbol{k})O_W^\nu(t)|0\rangle, \tag{A8}$$

as a standard two-point correlation function, where vector states propagate between Euclidean time t and Euclidean time $t_y > t$. Ignoring finite volume interactions, a standard application of the Parisi [49] and Lepage [50] argument, shows that at fixed time t and large-time separations $t_y - t$, the variance $\sigma^2_{M^{\mu\nu}_{f,W}}(t_y - t, t, \boldsymbol{k})$ of $M^{\mu\nu}_{f,W}(t_y - t, t, \boldsymbol{k})$ decreases exponentially as

$$\sigma^2_{M^{\mu\nu}_{f,W}}(t_y - t, t, \boldsymbol{k}) \propto e^{-2M^{\mathrm{PS}}_{\bar{f}f}(t_y - t)}, \tag{A9}$$

with $M^{\mathrm{PS}}_{\bar{f}f}$ the mass of the lightest pseudoscalar $\bar{f}\gamma^5 f$ state. Instead, the signal $M^{\mu\nu}_{f,W}(t_y - t, t, \boldsymbol{k})$ scales asymptotically as

$$M^{\mu\nu}_{f,W}(t_y - t, t, \boldsymbol{k}) \propto e^{-E_V(\boldsymbol{k})(t_y - t)},$$
$$E_{f,V}(\boldsymbol{k}) = \sqrt{M^2_{f,V} + |\boldsymbol{k}|^2}, \tag{A10}$$

where $M_{f,V}$ is the mass of the lightest vector state interpolated by $\hat{j}^{\mu}_{f,\mathrm{em}}(t_y, \boldsymbol{k})$. This implies the following asymptotic scaling of the signal-to-noise (S/N) ratio of $M^{\mu\nu}_{f,W}(t_y - t, t, \boldsymbol{k})$

$$\frac{M^{\mu\nu}_{f,W}(t_y - t, t, \boldsymbol{k})}{\sigma_{M^{\mu\nu}_{f,W}}(t_y - t, t, \boldsymbol{k})} \sim e^{-(E_{f,V}(\boldsymbol{k}) - M^{\mathrm{PS}}_{\bar{f}f})(t_y - t)}. \tag{A11}$$

Equations (A9)–(A11) enable us to understand the scaling of the error as we discuss in the following subsection. When $P = D_s$, we have $M_{s,V} = M_{\phi} \simeq 1$ GeV, $M_{c,V} = M_{J/\Psi} \simeq 3.1$ GeV, $M^{\mathrm{PS}}_{\bar{s}s} = M_{\eta_{ss'}} \simeq 0.69$ GeV and $M^{\mathrm{PS}}_{\bar{c}c} = M_{\eta_c} \simeq 2.98$ GeV. We underline that Eqs. (A9)–(A11) only hold for large time separations $t_y - t$.

1. Analysis of the scaling of the signal-to-noise ratio of $C^{\mu\nu;2}_{f,W}$

We now have all the necessary ingredients to understand the scaling of the S/N ratio of $C^{\mu\nu;2}_{f,W}(t)$. To this end, we define a time, t_{cut}, such that for $t_y - t > t_{\mathrm{cut}}$ the asymptotic formulas in Eqs. (A9)–(A11) hold, i.e. both $M^{\mu\nu}_{f,W}(t_y - t, t, \boldsymbol{k})$ and $\sigma^2_{M^{\mu\nu}_{f,W}}(t_y - t, t, \boldsymbol{k})$ are dominated by the contributions from the lowest-energy vector and pseudoscalar intermediate states respectively:

$$M^{\mu\nu}_{f,W}(t_y - t, t, \boldsymbol{k}) \equiv \sum_{n=1} A_{f,n} e^{-E_{f,n}(\boldsymbol{k})(t_y - t)} + A_{f,0} e^{-E_{f,V}(\boldsymbol{k})(t_y - t)} \underset{t_y - t > t_{\mathrm{cut}}}{\simeq} A_{f,0} e^{-E_V(\boldsymbol{k})(t_y - t)} \tag{A12}$$

$$\sigma^2_{M^{\mu\nu}_{f,W}}(t_y - t, t, \boldsymbol{k}) \equiv \sum_{n=1} B^2_{f,n} e^{-M_{f,n}(t_y - t)} + B^2_{f,0} e^{-2M^{\mathrm{PS}}_{\bar{f}f}(t_y - t)} \underset{t_y - t > t_{\mathrm{cut}}}{\simeq} B^2_{f,0} e^{-2M^{\mathrm{PS}}_{\bar{f}f}(t_y - t)}, \tag{A13}$$

where $E_{f,n}(\boldsymbol{k}) > E_{f,V}(\boldsymbol{k})$ and $M_{f,n} > 2M^{\mathrm{PS}}_{\bar{f}f}$ for $n \geq 1$. We thus have[13]

$$C^{\mu\nu;2}_{f,W}(t, \boldsymbol{k}) \simeq -i \left[\sum_{n=1} A_{f,n} e^{E_{f,n}(\boldsymbol{k})t} \int_t^{t_{\mathrm{cut}}} dt_y e^{-(E_{f,n}(\boldsymbol{k}) - E_{\gamma})t_y} + A_{f,0} e^{E_{f,V}(\boldsymbol{k})t} \int_t^{T/2} dt_y e^{-(E_{f,V}(\boldsymbol{k}) - E_{\gamma})t_y} \right] \tag{A14}$$

$$\sigma_{C^{\mu\nu;2}_{f,W}}(t, \boldsymbol{k}) = \int_t^{T/2} dt_y e^{E_{\gamma} t_y} \sigma_{M^{\mu\nu}_{f,W}}(t_y - t, t, \boldsymbol{k}) \simeq \int_t^{t_{\mathrm{cut}}} dt_y \sqrt{\sum_{n=0} [B^2_{f,n} e^{M_{f,n} t} e^{-(M_{f,n} - 2E_{\gamma})t_y}]} + B_{f,0} e^{M^{\mathrm{PS}}_{\bar{f}f} t} \int_{t_{\mathrm{cut}}}^{T/2} dt_y e^{-(M^{\mathrm{PS}}_{\bar{f}f} - E_{\gamma})t_y}. \tag{A15}$$

Since for each value of the photon's energy, $E_{\gamma} = |\boldsymbol{k}|$, one has $E_{f,n}(\boldsymbol{k}) > E_{f,V}(\boldsymbol{k}) > E_{\gamma}$, the integral over t_y in Eq. (A14) is always convergent and dominated by the

---

[13]In writing Eq. (A15) we are assuming that the values of $M^{\mu\nu}_{f,W}(t_y - t, t, \boldsymbol{k})$ at different times t_y are fully correlated, which is a fairly good assumption given that the different times are typically evaluated using the same set of gauge configurations. However, the main result obtained in this appendix, namely the exponential growth of the error in Eq. (A16), does not depend upon this assumption.

time region where t_y is close to t. Indeed, there are no intermediate states lighter than the energy of the external states. However, this is not always the case for the standard deviation $\sigma_{C^{\mu\nu;2}_{f,W}}(t, \boldsymbol{k})$. When passing the threshold value $E_{\gamma} = M^{\mathrm{PS}}_{\bar{f}f}$ the leading exponential contribution in Eq. (A15) (the term proportional to $B_{f,0}$) grows asymptotically with t_y and is only regularized by the finite time extent T of the lattice. In this case, from the leading exponential term in Eq. (A15) one has that the divergent part of the error for $E_{\gamma} > M^{\mathrm{PS}}_{\bar{f}f}$ is given by

$$\sigma_{C_{f,W}^{\mu\nu;2}}(t,\boldsymbol{k}) \simeq B_{f,0} e^{M_{\bar{f}f}^{\mathrm{PS}}t} \int_t^{T/2} dt_y e^{-(M_{\bar{f}f}^{\mathrm{PS}}-E_\gamma)t_y}$$

$$= B_{f,0} \frac{e^{E_\gamma t}}{(E_\gamma - M_{\bar{f}f}^{\mathrm{PS}})} \left[e^{(E_\gamma - M_{\bar{f}f}^{\mathrm{PS}})(T/2-t)} - 1 \right]. \quad (A16)$$

The prefactor $e^{E_\gamma t}$ in Eq. (A16) is irrelevant since it does not contribute to $R_W^{\mu\nu}$ [see Eq. (9)] and thus to the hadronic tensor $H_W^{\mu\nu}$.

The reason behind the behavior described by Eqs. (A14)–(A16) is that the kernel function $e^{E_\gamma t_y}$, accounting for the propagation of the photon, weights the different regions in t_y in different ways, giving an exponential enhancement at large times t_y, which are therefore noisier. For real photon emission, the kernel $e^{E_\gamma t_y}$ never gives rise to a divergent integral in Eq. (A14), since the propagating vector states have nonzero three-momentum $\boldsymbol{k}$ so that $E_{f,V}(\boldsymbol{k}) > E_\gamma$ [see Eq. (A10)]. However, the states propagating in $\sigma_{M_{f,W}^{\mu\nu}}^2(t_y - t, t, \boldsymbol{k})$ are at rest, and when $E_\gamma > M_{\bar{f}f}^{\mathrm{PS}}$, the leading exponential contribution proportional to $\int dt_y e^{(E_\gamma - M_{\bar{f}f}^{\mathrm{PS}})t_y}$ in Eq. (A16) becomes divergent in the limit $T \to \infty$.

2. Numerical checks

For the D_s meson studied in this paper, the threshold value of $x_\gamma = 2E_\gamma/M_{D_s}$ above which the error starts to grow asymptotically is, according to Eq. (A16), given by

$$x_\gamma^{th} = 2 \frac{M_{\eta_{ss'}}}{M_{D_s}} \simeq 0.7. \quad (A17)$$

For $x_\gamma > x_\gamma^{th}$ the error will increase only in the contribution to $C_W^{\mu\nu}(t,\boldsymbol{k})$ where the photon is emitted from the strange quark, because for the emission from the charm quark, one has $M_{\bar{c}c}^{\mathrm{PS}} = M_{\eta_{cc'}} \simeq 3$ GeV, and the corresponding threshold value of x_γ is well beyond the physical region explored $x_\gamma \leq 1$.

The total error on the strange-quark contribution to $R_W^{\mu\nu}(t,\boldsymbol{k}) \equiv R_W^{\mu\nu}(t,\boldsymbol{k},0)$ [see Eq. (16)] for small times t can be modelled as

$$\sigma_{R_W^{\mu\nu}}(t,\boldsymbol{k}) = A_{R_W^{\mu\nu}} + \frac{B_{R_W^{\mu\nu}}}{|E_\gamma - M_{\eta_{ss'}}|} e^{(E_\gamma - M_{\eta_{ss'}})(T/2-t)}, \quad (A18)$$

where $A_{R_W^{\mu\nu}}$ is a *background noise* term, which we take as being independent from E_γ. The contribution $A_{R_W^{\mu\nu}}$ to the noise arises from the nondivergent contributions to the noise in Eq. (A14) as well as those coming from the first time ordering, $t > t_y$, in Eq. (A1). Assuming that at $x_\gamma = 0.8$ the error is large enough such that the term $A_{R_W^{\mu\nu}}$ is negligible compared to the one proportional to $B_{R_W^{\mu\nu}}$, we can directly test Eq. (A18) against our numerical data. This is shown in Fig. (13) where the error on the strange-quark contribution to $R_V^{12}(t,x_\gamma) \equiv R_V^{12}(t,\boldsymbol{k}(x_\gamma))$ is plotted as a function of $x_\gamma \geq 0.8$ for two different times $t/a = 2, 3$. As
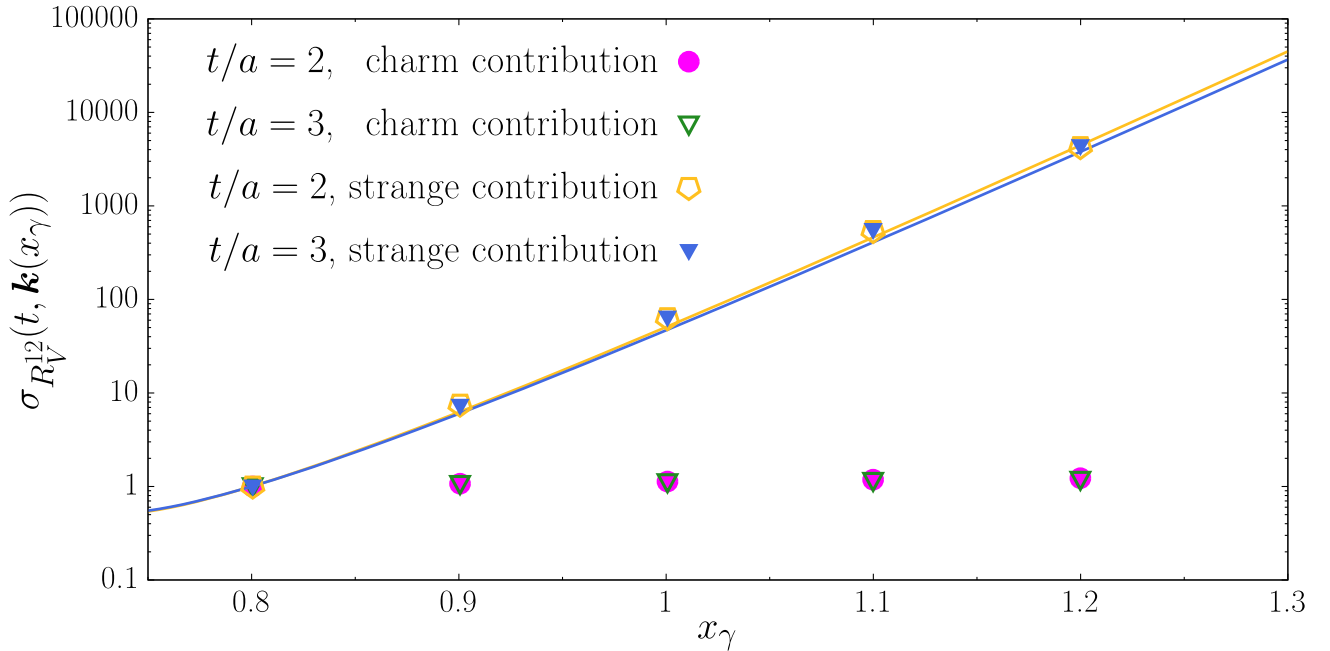

FIG. 13. The statistical error on the strange- and charm-quark contribution to $R_W^{\mu\nu}(t,\boldsymbol{k})$, with $\mu = 1$, $\nu = 2$ and $W = V$, is plotted as a function of x_γ for two different times $t/a = 2, 3$. The orange and blue curves correspond to the theoretical prediction of Eq. (A18) with $A_{R_W^{\mu\nu}} = 0$. Both the theoretical predictions and the numerical data have been rescaled in such a way that at $x_\gamma = 0.8$ the error is exactly one.

it is clear from the figure, the data are in remarkably good agreement with the theoretical prediction.

We conclude this appendix with a remark concerning the possibility of extending the calculation of F_V and F_A to the decays of D_d and B_u mesons over the full kinematical range, which is of even greater interest for phenomenology. In light of the above discussion, for these heavy-light mesons the threshold value of the photon energy E_γ above which the errors will start to exhibit the exponential behavior shown in Eq. (A16), is given by the pion mass M_π. This means that intrinsically large statistical fluctuations are to be expected in $C_W^{\mu\nu}(t, \boldsymbol{k})$ already at very small values of x_γ. In this case, a possible step towards avoiding the S/N problem, consists in evaluating the integral over t_y in Eq. (A1) on a reduced time interval $t_y \in [0, t_{\mathrm{cut}}]$, and then checking for convergence of the result as a function of t_{cut}. In this way one can expect to avoid including in the integration large values of t_y which do not contribute

substantially to the signal (which is dominated by the region of times t_y close to t) but which are responsible for the exponential increase of the error.

However, such approach requires the computation of the Euclidean three points function

$$M_W^{\mu\nu}(t_y, t; \boldsymbol{k}, \boldsymbol{p}) = \langle 0|\hat{T}[j_W^\nu(t)\hat{j}_{\mathrm{em}}^\mu(t_y, \boldsymbol{k})\hat{\phi}_P^\dagger(0, \boldsymbol{p})]|0\rangle, \quad \text{(A19)}$$

for different values of t and for all values t_y. In this way it is later possible to perform the integral over t_y for each value of t. Computations at several values of t need to be performed in order to verify that the ground state has been isolated. This makes the approach more expensive than computing $C_W^{\mu\nu}$ in Eq. (8) directly, which can be done for all values of t at the cost of a single *sequential propagator*. Whether such an extra cost for heavy-light mesons is offset by a significant improvement in accuracy remains to be seen. We plan to investigate this in the future.

APPENDIX B: RESULTS AND CORRELATION MATRICES FOR $F_A(x_\gamma)$ AND $F_V(x_\gamma)$

F_A correlation matrix

x_γ	F_A	Δ_{F_A}
0.1	0.08129	0.00538
0.2	0.07153	0.00406
0.3	0.06408	0.00330
0.4	0.05824	0.00282
0.5	0.05337	0.00213
0.6	0.04953	0.00243
0.7	0.04626	0.00309
0.8	0.04325	0.00325
0.9	0.04332	0.00827
1.0	0.04893	0.02291

1.00000	0.93275	0.90319	0.87687	0.83165	0.76844	0.65813	0.39596	0.19820	0.05885
0.93275	1.00000	0.92220	0.91694	0.86874	0.80104	0.65870	0.40917	0.19818	0.06649
0.90319	0.92220	1.00000	0.91785	0.88262	0.82681	0.67405	0.43075	0.20483	0.04460
0.87687	0.91694	0.91785	1.00000	0.89968	0.84780	0.67133	0.42214	0.22359	0.06804
0.83165	0.86874	0.88262	0.89968	1.00000	0.86177	0.70806	0.46356	0.21540	0.04650
0.76844	0.80104	0.82681	0.84780	0.86177	1.00000	0.78497	0.54501	0.27262	0.08763
0.65813	0.65870	0.67405	0.67133	0.70806	0.78497	1.00000	0.65900	0.36929	0.16734
0.39596	0.40917	0.43075	0.42214	0.46356	0.54501	0.65900	1.00000	0.60339	0.35453
0.19820	0.19818	0.20483	0.22359	0.21540	0.27262	0.36929	0.60339	1.00000	0.59821
0.05885	0.06649	0.04460	0.06804	0.04650	0.08763	0.16734	0.35453	0.59821	1.00000

F_V correlation matrix

x_γ	F_V	Δ_{F_V}
0.1	−0.10483	0.00966
0.2	−0.08188	0.00284
0.3	−0.06428	0.00131
0.4	−0.05187	0.00085
0.5	−0.04307	0.00080
0.6	−0.03632	0.00078
0.7	−0.03157	0.00071
0.8	−0.02913	0.00101
0.9	−0.02966	0.00559
1.0	−0.03147	0.01521

1.00000	0.88397	0.76281	0.62931	0.41384	0.24756	0.20298	0.08518	−0.01028	−0.02871
0.88397	1.00000	0.92314	0.76805	0.49098	0.31933	0.19618	0.08374	0.01045	−0.02545
0.76281	0.92314	1.00000	0.88045	0.59188	0.43306	0.23283	0.09787	0.03337	−0.01943
0.62931	0.76805	0.88045	1.00000	0.82870	0.61088	0.44651	0.20618	0.08193	0.02915
0.41384	0.49098	0.59188	0.82870	1.00000	0.68718	0.59022	0.29135	0.13671	0.08414
0.24756	0.31933	0.43306	0.61088	0.68718	1.00000	0.61811	0.38090	0.21946	0.14966
0.20298	0.19618	0.23283	0.44651	0.59022	0.61811	1.00000	0.69088	0.45154	0.29618
0.08518	0.08374	0.09787	0.20618	0.29135	0.38090	0.69088	1.00000	0.79170	0.56277
−0.01028	0.01045	0.03337	0.08193	0.13671	0.21946	0.45154	0.79170	1.00000	0.75941
−0.02871	−0.02545	−0.01943	0.02915	0.08414	0.14966	0.29618	0.56277	0.75941	1.00000

APPENDIX C: ANALYSIS OF SINGLE-POLE PARAMETRIZATIONS FOR $F_A(x_\gamma)$ AND $F_V(x_\gamma)$

Single-pole dominance, sometimes called vector-meson dominance (VMD) in the literature, is a model used to describe the momentum behavior of form factors, as determined by the propagation of the nearest internal resonance contributing to the amplitude. In this appendix we fit the data from our nonperturbative lattice computation of $F_A(x_\gamma)$ and $F_V(x_\gamma)$, to check the validity of such a parametrization. After demonstrating that a pure VMD Ansatz is not consistent with our results for the form factors, we propose a simple extension of the parametrization that can fit our data with good precision over the whole

kinematical range. This parametrization provides a simple and practical description of our data which can be used in future phenomenological analyses. We also check the stability of the fitted values of the residues of the singular pole terms in the parametrization [i.e. the C_W in Eq. (43)]. This is a necessary test in order to assess the validity of relating the fitted C_W to the $D_s^* \to D_s \gamma$ and $D_{s1} \to D_s \gamma$ decay amplitudes for the vector and axial channels respectively, as predicted by single-pole dominance.

VMD predictions are obtained by inserting a sum over intermediate states between the two operators in the correlation function defining $H_W^{\mu\nu}(k, p)$ in Eq. (1) and approximating this sum by the contribution from the nearest state. This approximation is also appropriately called single-pole dominance. For the vector and axial components of the weak current the nearest internal states are the D_s^* and D_{s1} mesons respectively, contributing to the time-ordering in which the electromagnetic current acts on the initial meson D_s at an earlier time than that at which the weak current is inserted, i.e. $t_y < 0$ in Eq. (8). Thus, by assuming single-pole dominance, we obtain the following parametrization for the momentum behavior of the form factors[14]:

$$
\begin{aligned}
F_A(\boldsymbol{k}) &= \frac{C_A'}{E_{D_{s1}}(\boldsymbol{k})(E_{D_{s1}}(\boldsymbol{k}) + E_\gamma - E)} \\
&= \frac{C_A'}{\sqrt{M_{D_{s1}}^2 + |\boldsymbol{k}|^2}\left(\sqrt{M_{D_{s1}}^2 + |\boldsymbol{k}|^2} + |\boldsymbol{k}| - M_{D_s}\right)},
\end{aligned}
$$
$$(C1)$$

$$
\begin{aligned}
F_V(\boldsymbol{k}) &= \frac{C_V'}{E_{D_s^*}(\boldsymbol{k})(E_{D_s^*}(\boldsymbol{k}) + E_\gamma - E)} \\
&= \frac{C_V'}{\sqrt{M_{D_s^*}^2 + |\boldsymbol{k}|^2}\left(\sqrt{M_{D_s^*}^2 + |\boldsymbol{k}|^2} + |\boldsymbol{k}| - M_{D_s}\right)},
\end{aligned}
$$
$$(C2)$$

where $M_{D_{s1}}$ and $M_{D_s^*}$ are the masses of the D_{s1} and D_s^* mesons respectively and C_A' and C_V' are constant coefficients with the dimension of energy squared. By dividing both the numerator and denominator of Eqs. (C1) and (C2) by $M_{D_s}^2$ and expressing $|\boldsymbol{k}|$ in terms of x_γ as $|\boldsymbol{k}| = \frac{x_\gamma M_{D_s}}{2}$, we obtain

$$
F_A(x_\gamma) = \frac{C_A}{\sqrt{R_{D_{s1}}^2 + \frac{x_\gamma^2}{4}}\left(\sqrt{R_{D_{s1}}^2 + \frac{x_\gamma^2}{4}} + \frac{x_\gamma}{2} - 1\right)}, \quad (C3)
$$

$$
F_V(x_\gamma) = \frac{C_V}{\sqrt{R_{D_s^*}^2 + \frac{x_\gamma^2}{4}}\left(\sqrt{R_{D_s^*}^2 + \frac{x_\gamma^2}{4}} + \frac{x_\gamma}{2} - 1\right)}, \quad (C4)
$$

where $C_{\{A,V\}} = \frac{C'_{\{A,V\}}}{M_{D_s}^2}$ and $R_{\{D_{s1}, D_s^*\}} = \frac{M_{\{D_{s1}, D_s^*\}}}{M_{D_s}}$ are now dimensionless parameters. By inserting the values $M_{D_{s1}} = 2460$ MeV, $M_{D_s^*} = 2112$ MeV and $M_{D_s} = 1968$ MeV, taken from the PDG [51], we obtain the ratios $R_{D_{s1}} = 1.25$ and $R_{D_s^*} = 1.073$. Thus, Eqs. (C3) and (C4) describe the momentum dependence, as predicted by VMD, for the axial and vector form factors, and also for the contributions corresponding to the emission of the photon from the charm and strange quarks separately. In order to check the validity of the VMD prediction, we fit our lattice results to the parametrization of Eqs. (C3) and (C4), with C_A and C_V taken as free parameters to be determined from the fit.[15] The results of these fits are shown in the plots in Fig. 14. It is clear from the figure, and confirmed by the corresponding high values of $\chi^2/\text{d.o.f.}$, that the results of the fit are in general very poor. The only exception is the VMD fit for the total vector form factor $F_V(x_\gamma)$, which proves to be a good fit of our data.

Since the pure VMD fit, with only one free parameter, fails to describe our lattice results for the form factors, we now introduce a more general Ansatz; one that represents the Laurent expansion of a function around a pole:

$$
F_W(x_\gamma) = \frac{C_W}{\sqrt{R_W^2 + \frac{x_\gamma^2}{4}}\left(\sqrt{R_W^2 + \frac{x_\gamma^2}{4}} + \frac{x_\gamma}{2} - 1\right)} + B_W + D_W x_\gamma,
$$
$$(C5)$$

where we have included corrections up to linear terms in x_γ, with C_W, R_W, B_W, and D_W being free parameters to be determined from the fit. In Eq. (C5), the difference of the parameters R_W from the VMD values $R_{D_{s1}} = 1.25$ and $R_{D_s^*} = 1.073$, partially accounts for the contributions from heavier internal states. The free parameters B_W and D_W, that describe the first two nonsingular terms of the Laurent expansion of a function around a pole, are also expected to encode non-negligible contributions that are not included in the pure VMD description. In order to check for the stability of the residues C_A and C_V, and hence their interpretation in terms of the $D_{s1} \to D_s \gamma$ and $D_s^* \to D_s \gamma$ decay amplitudes, we have performed several fits of our data, based on the Ansatz of Eq. (C5), fixing on each occasion some of its parameters to their VMD values.[16] Specifically, the *CR* fit is performed by fixing

---

[14]Here and in the following, we employ the reference frame in which the initial D_s meson is at rest.

[15]All the fits of this analysis have been performed by minimizing the *correlated* χ^2.

[16]With the limited number of points for which we have results, it is not possible to perform fits with all four parameters left free to be determined by the fits as this results in overfitting.
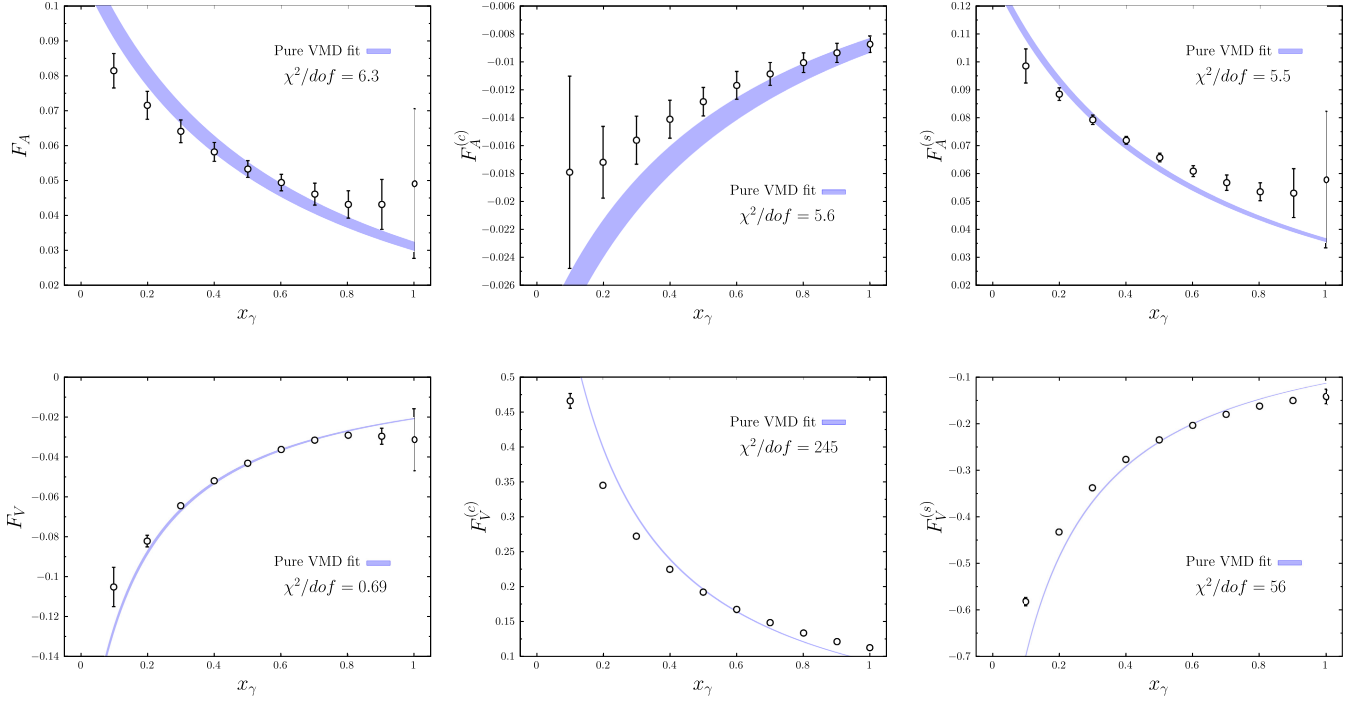
FIG. 14. The fit functions, corresponding to the pure VMD Ansatz of Eqs. (C3)–(C4), are plotted, along with the lattice data, for the axial channel (top panels), and for the vector channel (bottom panels).

$B_W = D_W = 0$, while the *CRB* fit is performed by setting only $D_W = 0$. The *CB* fit is obtained by fixing $D_W = 0$ and $R_W = R_{D_s^*}$ for the vector channel and $R_W = R_{D_{s1}}$ for the axial one. Finally the *CBD* fit, obtained by setting $R_W = R_{D_s^*}$ for the vector channel and $R_W = R_{D_{s1}}$ for the axial one, with the remaining three parameters determined by the fits. The results of these fits, for each form factor and for their individual charm and strange contributions, are reported in Table VIII.

From the table, we see that all the different Ansätze provide an adequate fit to our data for the axial channel, but we notice that the fitted values for the residue of the singular term, C_A, obtained from the *CR* fit are very different from those obtained from the fits with B_A as a free parameter. Although all three fits with B_A as a free parameter give consistent results for C_A, we avoid relating these results to the $D_{s1} \to D_s \gamma$ decay amplitude for two reasons. Firstly, because the value of C_A obtained from the *CR* fit, which is also a good fit to our data, is very different. Secondly, because of the presence in the axial channel, of another resonance, namely the $D_{s1}(2536)$ meson, with a mass which is only slightly above the nearest resonance, i.e. the $D_{s1}(2460)$ meson. Since the 76 MeV difference between the masses of the two resonances is so small, the fitted amplitude C_A could encode contributions coming from both of these internal states, resulting in an unreliable determination of the coupling $g_{D_{s1}D_s\gamma}$.

In the vector channel, we note that when fitting our results for $F_V^{(s)}$ and $F_V^{(c)}$ we need to include the presence of

the constant terms $B_V^{(s)}$ and $B_V^{(s)}$ to obtain low values of $\chi^2/\text{d.o.f.}$. However, we find that in the sum of the charm and strange-quark contributions to F_V, the individual nonsingular terms cancel almost exactly, i.e. $B_V^{(c)} \simeq -B_V^{(s)}$. As a result, the simple single-pole Ansatz, with B_V and D_V fixed to zero, already provides a good fit of the data for the total vector form factor F_V. In the fits with a low value of $\chi^2/\text{d.o.f.}$, i.e. all the fits except the *CR* fit to $F_V^{(s)}$ and $F_V^{(c)}$, the value of R_V is remarkably close to that from the pure VMD Ansatz, i.e. $R_{D_s^*} = 1.073$, differing by less than 3%, and the values of C_V are all very similar. The similarities between the values of R_V and $R_{D_s^*}$, and the stability of the values of the C_V parameter allow us to relate the fitted value for the residue of the pole term, C_V, to the $D_s^* \to D\gamma$ decay amplitude, and to its characteristic coupling $g_{D_s^*D_s\gamma}$, using the pole-dominance relation

$$C_V = -\frac{M_{D_s^*} f_{D_s^*} g_{D_s^*D_s\gamma}}{2M_{Ds}}. \tag{C6}$$

In order to determine $g_{D_s^*D_s\gamma}$ and its individual strange and charm-quark contributions, we use the values of C_V from the fits with low values of $\chi^2/\text{d.o.f.}$ and take the value $f_{D_s^*} = 268.8(6.6)$ MeV from the lattice calculation of Ref. [47]. The corresponding estimates of the couplings are reported in Table VII. Averaging the values of the couplings reported in the table, we obtain our final estimates

TABLE VIII. Values of the fit parameters for each form factor, and for their individual charm and strange-quark contributions, as determined from the different fits based on the Ansatz of Eq. (C5).

	F_A fitted parameters				
	C_A	R_A	B_A	D_A	χ^2/d.o.f.
CR fit	0.0518(30)	1.413(30)	0 (fixed)	0 (fixed)	0.41
CRB fit	0.0229(76)	1.242(59)	0.0185(67)	0 (fixed)	0.04
CB fit	0.0239(20)	1.25 (fixed)	0.0176(18)	0 (fixed)	0.03
CBD fit	0.0246(51)	1.25 (fixed)	0.016(11)	0.002(10)	0.04

	$F_A^{(c)}$ fitted parameters				
	C_A	R_A	B_A	D_A	χ^2/d.o.f.
CR fit	−0.0135(10)	1.453(59)	0 (fixed)	0 (fixed)	0.23
CRB fit	−0.0075(26)	1.27(11)	−0.0025(14)	0 (fixed)	0.08
CB fit	−0.00696(88)	1.25 (fixed)	−0.00280(47)	0 (fixed)	0.07
CBD fit	−0.0068(23)	1.25 (fixed)	−0.0030(37)	0.0002(22)	0.08

	$F_A^{(s)}$ fitted parameters				
	C_A	R_A	B_A	D_A	χ^2/d.o.f.
CR fit	0.0662(56)	1.423(36)	0 (fixed)	0 (fixed)	0.24
CRB fit	0.031(17)	1.26(10)	0.021(13)	0 (fixed)	0.09
CB fit	0.0298(18)	1.25 (fixed)	0.0215(31)	0 (fixed)	0.08
CBD fit	0.0309(87)	1.25 (fixed)	0.018(22)	0.003(18)	0.08

	F_V fitted parameters				
	C_V	R_V	B_V	D_V	χ^2/d.o.f.
CR fit	−0.01792(76)	1.091(11)	0 (fixed)	0 (fixed)	0.45
CRB fit	−0.0193(23)	1.100(19)	0.0018(28)	0 (fixed)	0.47
CB fit	−0.01619(58)	1.073 (fixed)	−0.0017(16)	0 (fixed)	0.66
CBD fit	−0.0153(16)	1.073 (fixed)	−0.0064(77)	0.0045(71)	0.75

	$F_V^{(c)}$ fitted parameters				
	C_V	R_V	B_V	D_V	χ^2/d.o.f.
CR fit	0.1144(13)	1.2001(41)	0 (fixed)	0 (fixed)	53
CRB fit	0.0624(15)	1.0809(43)	0.0369(14)	0 (fixed)	0.31
CB fit	0.05971(55)	1.073 (fixed)	0.03886(82)	0 (fixed)	0.76
CBD fit	0.0579(13)	1.073 (fixed)	0.0466(45)	−0.0055(33)	0.43

	$F_V^{(s)}$ fitted parameters				
	C_V	R_V	B_V	D_V	χ^2/d.o.f.
CR fit	−0.1099(11)	1.1245(29)	0 (fixed)	0 (fixed)	11
CRB fit	−0.0792(24)	1.0794(37)	−0.0367(31)	0 (fixed)	1.8
CB fit	−0.07571(96)	1.073 (fixed)	−0.0410(17)	0 (fixed)	1.8
CBD fit	−0.0759(16)	1.073 (fixed)	−0.0399(69)	−0.0011(67)	2.1

TABLE IX. Predictions for the $g_{D_s^* D_s \gamma}$ coupling, and for its individual charm and strange contributions, as obtained from our various fits, based on the Ansatz of Eq. (C5). Only results from fits with a low value of $\chi^2/\mathrm{d.o.f.}$ have been included.

	CR fit	CRB fit	CB fit	CBD fit
$g_{D_s^* D_s \gamma}$ [GeV^{-1}]	0.1223(51)	0.130(14)	0.1123(49)	0.106(11)
$g_{D_s^* D_s \gamma}^{(s)}$ [GeV^{-1}]	$\cdots$	0.546(20)	0.525(15)	0.526(17)
$g_{D_s^* D_s \gamma}^{(c)}$ [GeV^{-1}]	$\cdots$	$-0.429(14)$	$-0.414(11)$	$-0.402(13)$

$$g_{D_s^* D_s \gamma} = 0.1177 \pm 0.0048_{\text{stat}} \pm 0.012_{\text{syst}} \text{ GeV}^{-1}, \quad (C7)$$

$$g_{D_s^* D_s \gamma}^{(s)} = 0.532 \pm 0.010_{\text{stat}} \pm 0.011_{\text{syst}} \text{ GeV}^{-1}, \quad (C8)$$

$$g_{D_s^* D_s \gamma}^{(c)} = -0.4150 \pm 0.0073_{\text{stat}} \pm 0.014_{\text{syst}} \text{ GeV}^{-1}, \quad (C9)$$

where we include half of the maximum dispersion among the values obtained from the different fits as the systematic uncertainty. In Sec. V, we compare these results to two previous estimates of the same quantities, obtained either through a direct lattice computation [21] or by using LCSR at next-to-leading order [22].

[1] M. Bychkov *et al.*, New Precise Measurement of the Pion Weak Form Factors in $pi^+ \to e^+ \nu \gamma$ Decay, Phys. Rev. Lett. **103**, 051802 (2009).

[2] S. Adler *et al.* E787 Collaboration, Measurement of Structure Dependent $K^+ \to \mu^+ \nu_\mu \gamma$ Decay, Phys. Rev. Lett. **85**, 2256 (2000).

[3] F. Ambrosino *et al.* KLOE Collaboration, Precise measurement of $\Gamma(K \to e\nu(\gamma))/\Gamma(K \to \mu\nu(\gamma))$ and study of $K \to e\nu\gamma$, Eur. Phys. J. C **64**, 627 (2009).

[4] V. I. Kravtsov *et al.* OKA Collaboration, Measurement of the $K^+ \to \mu^+ \nu_\mu \gamma$ decay form factors in the OKA experiment, Eur. Phys. J. C **79**, 635 (2019).

[5] V. A. Duk *et al.* ISTRA+ Collaboration, Extraction of kaon formfactors from $K^- \to \mu^- \nu_\mu \gamma$ decay at ISTRA + setup, Phys. Lett. B **695**, 59 (2011).

[6] J-PARC E36 Collaboration, Measurement of structure dependent radiative $K^+ \to e^+ \nu \gamma$ decays using stopped positive kaons, Phys. Lett. B **826**, 136913 (2022).

[7] M. Ablikim *et al.* BESIII Collaboration, Search for the radiative leptonic decay $D^+ \to \gamma e^+ \nu_e$, Phys. Rev. D **95**, 071102 (2017).

[8] M. Ablikim *et al.* BESIII Collaboration, Search for the decay $D_s^+ \to \gamma e^+ \nu_e$, Phys. Rev. D **99**, 072002 (2019).

[9] A. Heller *et al.* Belle Collaboration, Search for $B^+ \to \ell^+ \nu_\ell \gamma$ decays with hadronic tagging using the full Belle data sample, Phys. Rev. D **91**, 112009 (2015).

[10] M. Gelb *et al.* Belle Collaboration, Search for the rare decay of $B^+ \to \ell^+ \nu_\ell \gamma$ with improved hadronic tagging, Phys. Rev. D **98**, 112016 (2018).

[11] A. Desiderio *et al.*, First lattice calculation of radiative leptonic decay rates of pseudoscalar mesons, Phys. Rev. D **103**, 014502 (2021).

[12] R. Frezzotti, M. Garofalo, V. Lubicz, G. Martinelli, C. T. Sachrajda, F. Sanfilippo, S. Simula, and N. Tantalo *et al.*, Comparison of lattice QCD + QED predictions for radiative leptonic decays of light mesons with experimental data, Phys. Rev. D **103**, 053005 (2021).

[13] C. Alexandrou *et al.*, Simulating twisted mass fermions at physical light, strange and charm quark masses, Phys. Rev. D **98**, 054518 (2018).

[14] C. Alexandrou *et al.* Extended Twisted Mass Collaboration, Ratio of kaon and pion leptonic decay constants with $N_f = 2 + 1 + 1$ Wilson-clover twisted-mass fermions, Phys. Rev. D **104**, 074520 (2021).

[15] C. Alexandrou *et al.* Extended Twisted Mass Collaboration, Quark masses using twisted-mass fermion gauge ensembles, Phys. Rev. D **104**, 074515 (2021).

[16] C. Alexandrou *et al.*, Lattice calculation of the short and intermediate time-distance hadronic vacuum polarization contributions to the muon magnetic moment using twisted-mass fermions, Phys. Rev. D **107**, 074506 (2023).

[17] D. Giusti, C. F. Kane, C. Lehner, S. Meinel, and A. Soni, High-precision determination of radiative-leptonic-decay form factors using lattice QCD: A study of methods, Phys. Rev. D **107**, 074507 (2023).

[18] G. P. Korchemsky, D. Pirjol, and T.-M. Yan, Radiative leptonic decays of B mesons in QCD, Phys. Rev. D **61**, 114510 (2000).

[19] D. Atwood, G. Eilam, and A. Soni, Pure leptonic radiative decays $B^\pm$, $D_s \to \ell \nu \gamma$ and the annihilation graph, Mod. Phys. Lett. A **11**, 1061 (1996).

[20] J.-C. Yang and M.-Z. Yang, Radiative leptonic decays of the charged B and D mesons including long-distance contribution, Mod. Phys. Lett. A **27**, 1250120 (2012).

[21] G. C. Donald, C. T. H. Davies, J. Koponen, and G. P. Lepage HPQCD Collaboration, Prediction of the D_s^* Width from a Calculation of its Radiative Decay in Full Lattice QCD, Phys. Rev. Lett. **112**, 212002 (2014).

[22] B. Pullin and R. Zwicky, Radiative decays of heavy-light mesons and the $f_{H,H^*,H_1}^{(T)}$ decay constants, J. High Energy Phys. 09 (2021) 023.

[23] J. Lyon and R. Zwicky, $A_{\rm CP}[D_{(s)}^{0,+} \to V\gamma]$ from large $\mathcal{O}_8$, Phys. Rev. D **106**, 053001 (2022).

[24] D. Guadagnoli, C. Normand, S. Simula, and L. Vittorio, From $D_s \to \gamma$ in lattice QCD to $B_s \to \mu\mu\gamma$ at high q^2, J. High Energy Phys. 07 (2023) 112.

[25] N. Carrasco, V. Lubicz, G. Martinelli, C. T. Sachrajda, N. Tantalo, C. Tarantino, and M. Testa, QED corrections to hadronic processes in lattice QCD, Phys. Rev. D **91**, 074506 (2015).

[26] J. Bijnens, G. Ecker, and J. Gasser, Radiative semileptonic kaon decays, Nucl. Phys. **B396**, 81 (1993).

[27] G. Gagliardi, F. Sanfilippo, S. Simula, V. Lubicz, F. Mazzetti, G. Martinelli, C. T. Sachrajda, and N. Tantalo, Virtual photon emission in leptonic decays of charged pseudoscalar mesons, Phys. Rev. D **105**, 114507 (2022).

[28] C. T. Sachrajda and G. Villadoro, Twisted boundary conditions in lattice simulations, Phys. Lett. B **609**, 73 (2005).

[29] J. M. Flynn, A. Juttner, C. T. Sachrajda, P. A. Boyle, and J. M. Zanotti, Hadronic form factors in lattice QCD at small and vanishing momentum transfer, J. High Energy Phys. 05 (2007) 016.

[30] Y. Iwasaki, Renormalization group analysis of lattice theories and improved lattice action: Two-dimensional nonlinear O(N) sigma model, Nucl. Phys. **B258**, 141 (1985).

[31] Alpha Collaboration, Lattice QCD with a chirally twisted mass term, J. High Energy Phys. 08 (2001) 058.

[32] R. Frezzotti and G. C. Rossi, Chirally improving Wilson fermions. 1. O(a) improvement, J. High Energy Phys. 08 (2004) 007.

[33] R. Frezzotti and G. C. Rossi, Chirally improving Wilson fermions. II. Four-quark operators, J. High Energy Phys. 10 (2004) 070.

[34] C. PatrignaniParticle Data Group, Review of particle physics, Chin. Phys. C **40**, 100001 (2016).

[35] K. Osterwalder and E. Seiler, Gauge field theories on the lattice, Ann. Phys. (N.Y.) **110**, 440 (1978).

[36] S. Borsanyi *et al.*, Leading hadronic contribution to the muon magnetic moment from lattice QCD, Nature (London) **593**, 51 (2021).

[37] Particle Data Group, Review of particle physics, Prog. Theor. Exp. Phys. **2020**, 083C01 (2020).

[38] HPQCD Collaboration, Charmonium properties from lattice QCD + QED: Hyperfine splitting, J/ψ leptonic width, charm quark mass, and a_μ^c, Phys. Rev. D **102**, 054511 (2020).

[39] R. Zhang, W. Sun, F. Chen, Y. Chen, M. Gong, X. Jiang, and Z. Liu, Annihilation diagram contribution to charmonium masses, Chin. Phys. C **46**, 043102 (2022).

[40] N. Carrasco *et al.*, $D^0 - \bar{D}^0$ mixing in the Standard Model and beyond from $N_f = 2$ twisted mass QCD, Phys. Rev. D **90**, 014502 (2014).

[41] H. Akaike, A new look at the statistical model identification, IEEE Trans. Autom. Control **19**, 716 (1974).

[42] E. T. Neil and J. W. Sitison, Improved information criteria for Bayesian model averaging in lattice field theory, arXiv:2208.14983.

[43] F. Bloch and A. Nordsieck, Note on the radiation field of the electron, Phys. Rev. **52**, 54 (1937).

[44] Y. Aoki *et al.*Flavour Lattice Averaging Group (FLAG) Collaboration, FLAG review 2021, Eur. Phys. J. C **82**, 869 (2022).

[45] C. Q. Geng, C. C. Lih, and W.-M. Zhang, Study of radiative leptonic D meson decays, Mod. Phys. Lett. A **15**, 2087 (2000).

[46] C.-D. Lu and G.-L. Song, Radiative leptonic decays of $D_s^\pm$ and $D^\pm$ mesons, Phys. Lett. B **562**, 75 (2003).

[47] ETM Collaboration, Masses and decay constants of $D_{(s)}^*$ and $B_{(s)}^*$ mesons with $N_f = 2 + 1 + 1$ twisted mass fermions, Phys. Rev. D **96**, 034524 (2017).

[48] R. Zwicky (private communication).

[49] G. Parisi, The strategy for computing the hadronic mass spectrum, Phys. Rep. **103**, 203 (1984).

[50] G. P. Lepage, The analysis of algorithms for lattice field theory, in *From Actions to Answers: Proceedings of the 1989 Theoretical Advanced Study Institute in Elementary Particle Physics* (1989), http://inspirehep.net/record/287173.

[51] K Agashe *et al.*Particle Data Group, Review of particle physics, Prog. Theor. Exp. Phys. **2022**, 083C01 (2022).